

# Accurate hybrid AUSMD type flux algorithm with generalized discontinuity sharpening reconstruction for two-fluid modeling



Te-Yao Chiu<sup>a</sup>, Yang-Yao Niu<sup>b,\*</sup>, Yi-Ju Chou<sup>a,\*</sup>

<sup>a</sup> Institute of Applied Mechanics, National Taiwan University, Taipei 10617, Taiwan

<sup>b</sup> Department of Aerospace Engineering, Tamkang University, New Taipei City 25137, Taiwan

## ARTICLE INFO

### Article history:

Available online 5 July 2021

### Keywords:

Two-fluid model

AUSMD

PVRS

Discontinuity sharpening

THINC scheme

## ABSTRACT

This paper presents a single-pressure-field two-fluid model with finite-volume discretization to solve the equations of motion of compressible multiphase flows. To capture the discontinuities caused by shock waves and fluid interfaces, we propose a generalized discontinuity sharpening technique that combines the conventional monotonic upstream scheme for conservation law (MUSCL) and tangent of hyperbola interface capturing (THINC) schemes. In addition, a slope ratio-weighted parameter,  $\zeta$ , is used to control the proportion of values reconstructed by MUSCL and THINC, and we show that the present method can retain sharp interfaces when the value of the parameter  $\beta$  in the THINC scheme is set ranging from 1.6 to 3.0. Fluxes across various interfaces are evaluated using a hybrid AUSMD-type flux algorithm, where the mass flux and pressure induced on the cell faces are calculated using an approximate Riemann solver. The accuracy and robustness of the proposed method are validated by solving a series of one- and two-dimensional single-phase flows. Furthermore, complex wave patterns arising from two-dimensional shock bubble/water-column interactions are examined, which indicate that compared with the existing schemes applied to two-fluid modeling, the proposed scheme significantly sharpens the interfaces and captures more details of the flow features. Finally, simulations of a three-dimensional example of the liquid jet crossflow are conducted. The proposed scheme shows more details of the fluid interface, including the interfacial instabilities on the windward side of the liquid jet and droplet formation due to the breakup phenomenon in the downstream of the crossflow, than the existing schemes.

© 2021 Elsevier Inc. All rights reserved.

## 1. Introduction

Compressible multiphase flows and many related subjects are gaining increasing relevance in various scientific disciplines and engineering applications. However, it is always challenging to perform analysis using analytical frameworks or experimental instruments due to the complexities and rapid transitions of multiphase phenomena. For this purpose, computation has become a powerful tool to elucidate the fundamental mechanisms behind complicated flow phenomena. The methodologies used for computing multiphase flows can be classified into two major categories: interface tracking [1–7] and interface capturing [8–15]. Interface tracking (e.g., the volume-of-fluid and level-set methods) introduces an indica-

\* Corresponding authors.

E-mail addresses: [yyniu@mail.tku.edu.tw](mailto:yyniu@mail.tku.edu.tw) (Y.-Y. Niu), [yjchou@iam.ntu.edu.tw](mailto:yjchou@iam.ntu.edu.tw) (Y.-J. Chou).

tor function to track the evolution of the interface. However, unless a special treatment is applied, these schemes usually suffer from interface smearing due to numerical diffusion in the discretized indicator function [16]. In contrast, interface capturing (e.g., a two-fluid model) applies the time- or spatial-averaged procedure [10,11] to equations of motion for carrier and disperse phases. In this approach, two sets of Euler/Navier-Stokes equations are used to describe the averaged macroscopic flow motion along with additional inter-phasic terms to model the exchange of mass, momentum, and energy between phases. The interface can be dynamically captured along with other physical properties by using standard numerical methods (e.g., finite-volume method). Because each phase has its own velocity and temperature, the model can simulate transient mechanical and thermal behaviors of different phases in the nonequilibrium state. Therefore, in this study, a two-fluid model is selected to model the complicated two-phase flow phenomena. However, difficulties arise from the fact that the inter-phasic terms, derived from the averaged procedure, are not in the conservative form (see Drew [11]). The major problematic feature of the two-fluid model is the nonhyperbolic characteristic resulting from the nonconservative inter-phasic terms, which leads to ill-posed problems. Because a weak solution does not exist in the resulting two-fluid system, numerical oscillations may occur near the shock waves, contact discontinuities, or interfaces due to a jump of the material properties [14]. To render the system of equations hyperbolic and stable, special mathematical treatments, such as interfacial pressure correlation [17] and virtual mass addition [18–20], have been developed.

Extensive studies have been conducted to determine the fluxes across the cell faces of a two-fluid model [12–15,21,22]. A representative implementation was conducted by Chang and Liou [12], who suggested that the fluid distribution inside a discrete mesh is locally “stratified”, such that the stratified flow model proposed by Stewart and Wendroff [23] is obeyed in each grid cell. In the stratified flow model, the nonconservative terms represent the pressure acting on the interface between the phases within a cell. Following this interpretation, the nonconservative terms can be discretized using the values reconstructed on the cell faces rather than the finite-difference method (e.g., central difference), which uses the values at the cell center. Adopting the concept of a stratified flow model, the cell boundary can be divided into four interfaces: gas-gas, liquid-liquid, gas-liquid, and liquid-gas. Chang and Liou [12] used AUSM+-up [24], which extends the AUSM+ [25] scheme along with the exact Riemann solver [26] to all-speed calculations, and evaluated the fluxes across the cell faces in the “same phases” (gas-gas and liquid-liquid) and “different phases” (gas-liquid or liquid-gas). This approach was proved to be accurate and robust. However, the exact Riemann solver typically requires many iterations in each time step, which is computationally expensive. Moreover, an analytical equation of the exact Riemann solver cannot be easily obtained when a complex equation of state is involved [12,26]. In this regard, Pandare and Luo [27] and Pandare et al. [28] considered the relative velocity between phases and added the volume fraction coupling and velocity-diffusion terms to the AUSM+-up scheme. These prevent the original AUSM+-up from obtaining the negative pressure in the region where strong shock waves interact with material interfaces without resorting to expensive Riemann solver. Houim and Oran [29] further used this scheme to the computations of compressible granular-gaseous flows. Recently, Niu [13] developed a hybrid flux algorithm based on the AUSMD scheme [30] to obtain the numerical flux on the cell interface. In that study, the mass flux and pressure induced on the cell boundaries were calculated using the primitive variable Riemann solver (PVRS) [31], which is less computationally expensive than the exact Riemann solver. Through several benchmark tests, Niu [13] demonstrated that, besides achieving the desired accuracy, the hybrid AUSMD scheme is more efficient than the other AUSM-type schemes incorporating the exact Riemann solver. This hybrid scheme was further applied by Niu and Wang [32] to a three-dimensional (3D) numerical study on the impact of liquid bubbles on solid walls.

In addition to the aforementioned methodologies used for determining fluxes, another key factor that affects the accuracy while solving a two-fluid system is the interpolation of the physical variables on the grid faces. To resolve the discontinuity without numerical oscillations, total variation diminishing (TVD) schemes, such as the monotonic upstream scheme for conservation law (MUSCL) [33], have been widely used to obtain values of physical variables on cell faces [12–15,22,27,32]. However, TVD schemes usually suffer from excessive numerical diffusion [15], making the interface indistinct. Therefore, for addressing problems in which surface tension plays an important role, such as droplets and bubbles, a “sharpening” procedure is necessary to reduce the numerical thickening and increase the accuracy of curvature estimation. In this regard, special treatments for the interface, such as artificial compression [34,35] and antidiffusion [36], have been developed to limit the interface thickening. Xiao et al. [16] proposed the tangent of hyperbola interface capturing (THINC) scheme, in which a simple hyperbolic tangent function is implemented to mimic the step-like profile of the volume-of-fluid (VOF) function in incompressible multiphase flows. They showed that the THINC scheme can adequately handle complex geometries. Then, Kitamura et al. [22], Pandare and Luo [27] used THINC to interpolate the volume fraction in a two-fluid model while reconstructing the other state variables using MUSCL. Although the interface could be significantly sharpened by THINC in these studies, there remain issues resulting from the reconstruction of the state variables using MUSCL. Because physical quantities other than the volume fraction usually comprise both discontinuous and continuous parts (i.e., shock waves and rarefaction fan, respectively), adopting the MUSCL scheme for determining these quantities can result in excessive diffusion around the shock wave even if it appropriately captures the rarefaction fan. Thus, the wave patterns generated by the shock wave can become indistinct in long-term calculations. These necessitates applying the sharpening procedure to all other physical variables, and not just the volume fraction. As an algebraic reconstruction, THINC can serve as a suitable scheme for this purpose and can be easily extended to all variables. However, application of THINC only to those state variables in which the shock wave and rarefaction fan coexist is problematic because the hyperbolic tangent function is too sharp to define the continuous profile of variables, which leads to the “square wave effect” phenomenon introduced by Tann et al. [37].

Recently, a successful approach to sharpen the discontinuity of state variables without generating the square wave effect has been proposed by Sun et al. [38]. They developed a boundary variation diminishing (BVD) algorithm to find the optimal reconstruction method between high-order TVD/polynomial-based schemes (e.g., high-order accurate weighted essentially nonoscillatory) and THINC to minimize the variations in the reconstructed values on the cell boundaries. It has been shown that the BVD algorithm can not only remove the numerical diffusion but also adequately capture detailed flow features. The BVD algorithm has been implemented for both single-phase [37,39,40] and multiphase flows [41,42]. More recently, it has been further extended to the unstructured grids to handle flows over complex geometries with high accuracy [43].

In this study, we propose an alternative approach, which exploits both THINC and MUSCL by automatically adjusting the weight of each method based on the sharpness of solutions. In our approach, through a slope-weighted parameter, the MUSCL scheme is mainly used to handle solutions with smooth changes, whereas THINC is used to capture discontinuous jumps. While the idea is similar to that of BVD, the present approach is formulated in a more straightforward manner and can be easily implemented. More importantly, while it has been shown that the BVD may cost about two times more CPU time than the typical TVD schemes [39], our numerical examples in two-dimensional cases show that the present method can be more computationally efficient. Moreover, following Niu [13], a hybrid AUSMD-type flux algorithm is used in the present scheme to calculate fluxes across a cell face in the same phases and different phases, where the mass flux and pressure are obtained using the PVRS. In this way, numerical stability can be achieved without sacrificing computational efficiency. Compared with existing methods [e.g. 33], the proposed scheme is more accurate and robust in capturing sharp variations of all physical variables, and numerical simulations can be conducted with high efficiency. Because the unstructured grids are not a topic of interest here, the implementation and demonstrations are focused only on structured grids.

The rest of this paper is organized as follows. In Section 2, the governing equations of the two-fluid model are described, followed by the details of the solution procedures. In Section 3, the results of single-phase and multiphase benchmark tests are presented along with a comparison between the proposed method and existing schemes. Finally, the concluding remarks are presented in Section 4.

## 2. Numerical methods

### 2.1. Two-fluid model

We consider a 3D compressible two-fluid model in which viscous terms and phase change between gas and liquid are neglected:

$$\frac{\partial \mathbf{Q}_k}{\partial t} + \frac{\partial \mathbf{E}_k}{\partial x} + \frac{\partial \mathbf{F}_k}{\partial y} + \frac{\partial \mathbf{G}_k}{\partial z} = \mathbf{S}_k^{\text{int}}, \quad (1)$$

where

$$\mathbf{Q}_k = \begin{bmatrix} \alpha\rho \\ \alpha\rho u \\ \alpha\rho v \\ \alpha\rho w \\ \alpha\rho E \end{bmatrix}_k, \quad \mathbf{E}_k = \begin{bmatrix} \alpha\rho u \\ \alpha\rho u^2 + \alpha p \\ \alpha\rho uv \\ \alpha\rho uw \\ \alpha\rho uH \end{bmatrix}_k, \quad (2)$$

and

$$\mathbf{F}_k = \begin{bmatrix} \alpha\rho v \\ \alpha\rho vu \\ \alpha\rho v^2 + \alpha p \\ \alpha\rho vw \\ \alpha\rho vH \end{bmatrix}_k, \quad \mathbf{G}_k = \begin{bmatrix} \alpha\rho w \\ \alpha\rho wu \\ \alpha\rho wv \\ \alpha\rho w^2 + \alpha p \\ \alpha\rho wh \end{bmatrix}_k, \quad \mathbf{S}_k^{\text{int}} = \begin{bmatrix} 0 \\ p^{\text{int}} \frac{\partial \alpha}{\partial x} \\ p^{\text{int}} \frac{\partial \alpha}{\partial y} \\ p^{\text{int}} \frac{\partial \alpha}{\partial z} \\ -p^{\text{int}} \frac{\partial \alpha}{\partial t} \end{bmatrix}_k, \quad (3)$$

where  $\alpha$  is the volume fraction of the fluid;  $\rho$  is the density;  $u$ ,  $v$ , and  $w$  are the velocity components in Cartesian coordinates;  $p$  is the pressure;  $E = e + \frac{1}{2}(u^2 + v^2 + w^2)$  is the total energy, where  $e$  is the internal energy;  $H = E + (\frac{p}{\rho})$  is the total enthalpy; and  $k = g, l$  indicates the gas and liquid phases. Similar to the single-phase notation,  $\mathbf{Q}_k$  is the conservation variable vector, and  $\mathbf{E}_k$ ,  $\mathbf{F}_k$ , and  $\mathbf{G}_k$  are the inviscid flux vectors in  $x-$ ,  $y-$ , and  $z-$  directions, respectively. In Eq. (3),  $\mathbf{S}_k^{\text{int}}$  represents the source terms corresponding to the interfacial interactions between phases. This system (Eqs. (1)-(3)) contains 16 unknown variables  $(\alpha, \rho, u, v, w, p, p^{\text{int}}, e)_k$ , whereas 12 equations with 10 differential equations and 2 equations of state are provided. This implies that four additional constraints are required for closing the system, which can be expressed as follows:

$$\alpha_g + \alpha_l = 1, \quad (4)$$

$$p_g = p_l = p, \quad (5)$$

**Table 1**  
Parameters of stiffened ideal gas equation of state.

Fluids	$\gamma$	$C_p \left( \frac{1}{\text{kg}\cdot\text{K}} \right)$	$p_\infty (\text{Pa})$
Water	1.93	8095.08	$1.16 \times 10^9$
Air	1.40	1004.50	0
Helium	1.65	5192.60	0
R22 refrigerant	1.25	456	0

$$p_g^{\text{int}} = p^{\text{int}} = p - \delta p^*, \quad (6)$$

$$p_l^{\text{int}} = p_g^{\text{int}} + \sigma \kappa. \quad (7)$$

Eq. (5) assumes that the bulk stress of each phase is in equilibrium, and Eq. (6) assumes that the interfacial pressure of gas should be in equilibrium with pressure at cell center. According to Stuhmiller [17] and Liou et al. [14], a correction term  $\delta p^*$  is added in Eq. (6) to preserve the hyperbolic characteristic of a two-fluid system:

$$\delta p^* = \xi \frac{\alpha_g \rho_g \alpha_l \rho_l}{\alpha_g \rho_l + \alpha_l \rho_g} |\vec{\mathbf{u}}_g - \vec{\mathbf{u}}_l|^2, \quad (8)$$

and  $\xi$  is usually set as 2.0 [12,14,15,22], which is adequate for most of our simulations. In Eq. (7),  $\sigma (\text{N m}^{-1})$  is the surface tension coefficient, and  $\kappa (\text{m}^{-1})$  is the curvature, which is positive toward the medium of higher density (i.e., liquid phase in the liquid-gas two phase system). Eq. (7) indicates that if the surface tension effect is involved, the pressure difference between the gas-liquid interface must satisfy the Young-Laplace formulation [44]. Substitution of Eq. (7) into (1) gives the momentum and energy equations of the liquid phase, which are written as,

$$\frac{\partial(\alpha \rho \mathbf{u})_l}{\partial t} + \nabla \cdot (\alpha \rho \mathbf{u} \mathbf{u})_l + \nabla \cdot (\alpha p)_l = p^{\text{int}} \nabla \alpha_l + \sigma \kappa \nabla \alpha_l, \quad (9)$$

and

$$\frac{\partial(\alpha \rho E)_l}{\partial t} + \nabla \cdot (\alpha \rho \mathbf{u} H)_l = -p^{\text{int}} \frac{\partial \alpha_l}{\partial t} - \sigma \kappa \frac{\partial \alpha_l}{\partial t}. \quad (10)$$

The last term of Eq. (9) is identical to the continuum surface force (CSF) model proposed by Brackbill et al. [45], which transforms the surface tension into a volumetric forcing term in the VOF method. However, the present study differs from Brackbill et al. [45] in that the energy contribution of the surface tension (the last term in Eq. (10)) is also taken into account. The energy difference caused by the surface tension can be thus considered, and the interfacial phenomena can be captured in a more correct manner. In our simulations,  $\kappa$  is computed using 9 stencils [45], and  $\sigma$  is treated as a constant.

## 2.2. Equation of state (EOS)

Here, we use the stiffened ideal gas equations of state (EOSSs) proposed by Harlow and Amsden [46], which are expressed as

$$p_k = \rho_k \frac{\gamma_k - 1}{\gamma_k} C_{p,k} T_k - p_{k\infty}, \quad (11)$$

$$e_k = \frac{C_{p,k}}{\gamma_k} T_k + \frac{p_{k\infty}}{\rho_k}, \quad (12)$$

$$a_k = \left[ \frac{\gamma_k (p_k + p_{k\infty})}{\rho_k} \right]^{\frac{1}{2}}, \quad (13)$$

where  $e_k$  is the internal energy per unit mass of fluid  $k$ ;  $a_k$  is the speed of sound; and  $\gamma_k$ ,  $C_{p,k}$ , and  $p_{k\infty}$  are the parameters required for specifying the thermodynamic properties of fluids. The constant values used in Eqs. (11)-(13) are listed in Table 1.

Note that the existence of a high  $p_\infty$  in water represents a weak connection between pressure and density. That is, the density of water remains almost constant even under a very large pressure. Although the model is relatively simple, it makes the two-fluid system stiff because of the large ratio of the eigenvalues between the liquid and gas phases ( $\sim O(10^3)$ ). Nevertheless, the stiffened gas model has been proven to be as accurate as other EOSSs, such as Tait's model for water and van der Waals's model for air, through several benchmark tests [47].

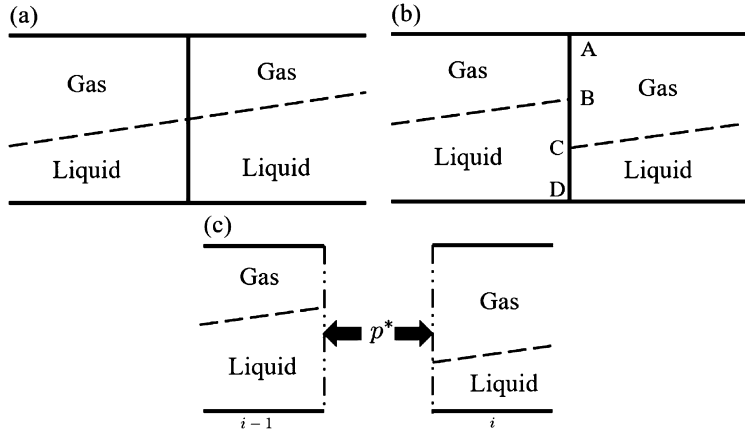


**Fig. 1.** Illustrations of the stratified flow model in which (a) the generic model proposed by Stewart and Wendroff [23], (b) discretization based on the stratified flow model and (c) the pressure across the cell face different phases (e.g., liquid-gas).

### 2.3. Numerical discretization

In this study, the two-fluid model is discretized using a stratified flow model [12,23] with a dimensional splitting operation. By omitting the phase index  $k$ , the semi-discretized form of a one-dimensional (1D) two-fluid model can be expressed as

$$\frac{V_i}{\Delta t} \Delta \mathbf{Q}_i + \mathbf{E}_{i+\frac{1}{2}} S_{i+\frac{1}{2}} - \mathbf{E}_{i-\frac{1}{2}} S_{i-\frac{1}{2}} = p_i^{\text{int}} \begin{bmatrix} 0 \\ \frac{\alpha_{i+\frac{1}{2}}^L - \alpha_{i-\frac{1}{2}}^R}{\Delta x_i} \\ -\left(\frac{\alpha^{n+1} - \alpha^n}{\Delta t}\right) \end{bmatrix}, \quad (14)$$

where  $i$  is the index of each cell,  $V_i$  is the cell volume,  $\Delta x_i$  is the grid spacing of cell  $i$ ,  $\Delta t$  is the computational time step,  $S_{i\pm\frac{1}{2}}$  indicates the facial area between cells  $i$  and  $i \pm 1$ , and  $\alpha_{i\pm\frac{1}{2}}^{L/R}$  indicates the volume fraction evaluated at the cell faces. As illustrated in Fig. 1a, this solver is based on the concept of a stratified flow model, proposed by Stewart and Wendroff [23], and the discretized stratified flow model (see Fig. 1b) divides the cell face into three interfaces: gas-gas (line AB), liquid-liquid (line CD), and liquid-gas (line BC). Hence, the total numerical flux across the cell interface  $\mathbf{E}_{i\pm\frac{1}{2}}$  can be expressed as

$$\mathbf{E}_{i\pm\frac{1}{2}} = \theta_{i\pm\frac{1}{2}}^{g-g} \mathbf{E}_{i\pm\frac{1}{2}}^{g-g} + \theta_{i\pm\frac{1}{2}}^{l-l} \mathbf{E}_{i\pm\frac{1}{2}}^{l-l} + \theta_{i\pm\frac{1}{2}}^{l-g} \mathbf{E}_{i\pm\frac{1}{2}}^{l-g}, \quad (15)$$

where the function  $\theta_{i\pm\frac{1}{2}}$  denotes the effective length of lines AB, BC, and CD on the cell faces, which can be defined as

$$\theta_{i\pm\frac{1}{2}}^{g-g} = \min(\alpha_{i\pm\frac{1}{2}}^{L,\text{gas}}, \alpha_{i\pm\frac{1}{2}}^{R,\text{gas}}), \quad (16)$$

$$\theta_{i\pm\frac{1}{2}}^{l-l} = \min(\alpha_{i\pm\frac{1}{2}}^{L,\text{liquid}}, \alpha_{i\pm\frac{1}{2}}^{R,\text{liquid}}), \quad (17)$$

$$\theta_{i\pm\frac{1}{2}}^{l-g} = \max(\Delta\alpha_g, 0), \quad (18)$$

$$\Delta\alpha_g = \alpha_{i\pm\frac{1}{2}}^{R,\text{gas}} - \alpha_{i\pm\frac{1}{2}}^{L,\text{gas}}. \quad (19)$$

### 2.4. Hybrid MUSCL-THINC reconstruction

This section presents details of calculating  $\mathbf{Q}_{i+\frac{1}{2}}^L$  and  $\mathbf{Q}_{i-\frac{1}{2}}^R$  at cell faces. Here  $\mathbf{Q}_{i\pm\frac{1}{2}}^{L/R}$  can be one of the primitive, conservative, or characteristic variables. In the present work, the reconstruction is applied to primitive variables. In two-fluid model, a general spatial discretization approach is MUSCL scheme [33] with a TVD (Total Variation Diminishing) slope limiter, which can be written as

$$\mathbf{Q}_{i+\frac{1}{2}}^L = \mathbf{Q}_i + \frac{1}{4} [(1 + \eta) \times \mathbf{smd}(q1, q2) + (1 - \eta) \times \mathbf{smd}(q2, q1)], \quad (20)$$

$$\mathbf{Q}_{i-\frac{1}{2}}^R = \mathbf{Q}_i - \frac{1}{4} [(1 + \eta) \times \mathbf{smd}(q_2, q_1) + (1 - \eta) \times \mathbf{smd}(q_1, q_2)], \quad (21)$$

where

$$q_1 = \mathbf{Q}_i - \mathbf{Q}_{i-1}, \quad (22)$$

$$q_2 = \mathbf{Q}_{i+1} - \mathbf{Q}_i. \quad (23)$$

In Eqs. (20) and (21), we set  $\eta = \frac{1}{3}$  to achieve third-order accuracy [33] and use the minmod slope limiter, **smd**, which is defined as

$$\mathbf{smd}(a, b) \equiv \max \{0, \min [a \times \mathbf{sgn}(b), b \times \mathbf{sgn}(a)]\} \times \mathbf{sgn}(a). \quad (24)$$

The major drawback of the MUSCL scheme is the associated excessive numerical diffusion. To address this issue, we use a sharpening technique, THINC [16]. The main concept of THINC lies in mimicking the step-like discontinuity by using a sigmoid, differentiable, and monotonic hyperbolic tangent function, expressed as

$$\mathbf{Q}_{i+\frac{1}{2}}^L = \mathbf{Q}_{\min} + \frac{\mathbf{Q}_{\max}}{2} \left[ 1 + \lambda \frac{\tanh(\beta) + A}{1 + A \tanh(\beta)} \right], \quad (25)$$

$$\mathbf{Q}_{i-\frac{1}{2}}^R = \mathbf{Q}_{\min} + \frac{\mathbf{Q}_{\max}}{2} (1 + \lambda A), \quad (26)$$

where

$$\mathbf{Q}_{\min} = \min(\mathbf{Q}_{i+1}, \mathbf{Q}_{i-1}), \quad (27)$$

$$\mathbf{Q}_{\max} = \max(\mathbf{Q}_{i+1}, \mathbf{Q}_{i-1}) - \mathbf{Q}_{\min}, \quad (28)$$

$$\lambda = \mathbf{sgn}(\mathbf{Q}_{i+1} - \mathbf{Q}_{i-1}), \quad (29)$$

and

$$A = \frac{1}{\tanh(\beta)} \frac{B}{\cosh(\beta) - 1}, \quad B = \exp [\lambda \beta (2C - 1)], \quad (30)$$

in which

$$C = \frac{\mathbf{Q}_i - \mathbf{Q}_{\min} + \varepsilon}{\mathbf{Q}_{\max} + \varepsilon}, \quad (31)$$

and a small value of  $\varepsilon$  is used to avoid the singularity in Eq. (31), which is set to  $10^{-20}$ . A constant coefficient,  $\beta$ , in Eq. (30) is used to control the sharpness of the hyperbolic tangent function and is usually set within 1.6–3.0. As mentioned in Section 1, when used to reconstruct a relatively smooth profile, THINC can yield erroneous results under the “square wave effect”. This indicates that the face values at the cell boundaries cannot be solely reconstructed by the THINC scheme, because except for the volume fraction, all physical quantities include both discontinuous and continuous parts in coexistence (i.e.,  $u, v, w, p, T$ ). Thus, we combine the MUSCL and THINC schemes with a weighted parameter,  $\zeta$ . In this method, MUSCL captures the continuous profile, whereas THINC captures the discontinuous profile. It should be noted that the so-called “hybrid MUSCL-THINC” scheme is employed only when the following condition is satisfied:

$$(\mathbf{Q}_{i+1} - \mathbf{Q}_i)(\mathbf{Q}_i - \mathbf{Q}_{i-1}) > 0, \quad (32)$$

and the face values evaluated by this scheme are modified as

$$\mathbf{Q}_{i+\frac{1}{2}}^L = (1 - \zeta) \times \mathbf{Q}_{i+\frac{1}{2}}^{L, \text{MUSCL}} + \zeta \times \mathbf{Q}_{i+\frac{1}{2}}^{L, \text{THINC}}, \quad (33)$$

$$\mathbf{Q}_{i-\frac{1}{2}}^R = (1 - \zeta) \times \mathbf{Q}_{i-\frac{1}{2}}^{R, \text{MUSCL}} + \zeta \times \mathbf{Q}_{i-\frac{1}{2}}^{R, \text{THINC}}, \quad (34)$$

where  $\mathbf{Q}_{i+\frac{1}{2}}^{L, \text{MUSCL}}$  and  $\mathbf{Q}_{i+\frac{1}{2}}^{L, \text{THINC}}$  are the face values reconstructed using MUSCL and THINC, respectively, and the weighted parameter  $\zeta$  is defined as

$$\zeta \equiv 1 - \min \left( \frac{\mathbf{Q}_{i+\frac{1}{2}}^{L, \text{MUSCL}} - \mathbf{Q}_{i-\frac{1}{2}}^{R, \text{MUSCL}} + \varepsilon}{\mathbf{Q}_{i+1} - \mathbf{Q}_i + \varepsilon}, \frac{\mathbf{Q}_{i+\frac{1}{2}}^{L, \text{MUSCL}} - \mathbf{Q}_{i-\frac{1}{2}}^{R, \text{MUSCL}} + \varepsilon}{\mathbf{Q}_i - \mathbf{Q}_{i-1} + \varepsilon} \right), \quad (35)$$

in which, again, a small value of  $\varepsilon$  is used to avoid singularity. When the local profile of the variables is monotonically upward or downward, we use Eqs. (33) and (34) to determine the reconstructed values on the cell faces. Otherwise, the

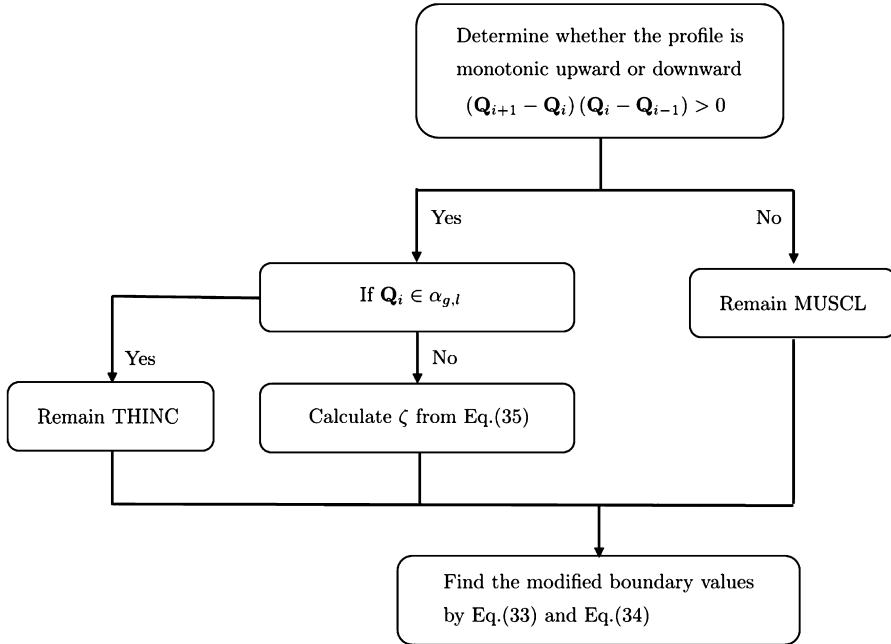


**Fig. 2.** Flow chart of the present hybrid MUSCL-THINC scheme.

MUSCL scheme is applied. The reconstruction of the volume fraction  $\alpha$  can be calculated using THINC alone, because the profile comprises only jump discontinuity. The weighted parameter  $\zeta$  in Eqs. (33)–(35) represents the slope ratio between the cell interface reconstructed by MUSCL and the adjacent cell centers. If  $\zeta$  is close to 0, meaning that the local profile is smooth, the calculation of the face values is dominated by MUSCL. Conversely, when  $\zeta$  is close to 1, meaning that the local profile is rather discontinuous, the face values are mainly determined by THINC. A complete sequence of the proposed method is summarized in the flowchart shown in Fig. 2.

## 2.5. Hybrid AUSMD type Riemann solver

Once the primitive variables on the left and right faces of the cell are determined, we make use of AUSMD to evaluate the flux across the cell faces. The basic concept for the AUSM-type scheme is to split the flux into convective and pressure terms [24,25,30], which can be expressed by

$$\mathbf{E}_{i \pm \frac{1}{2}} = \frac{1}{2} \left[ \dot{m}_{i \pm \frac{1}{2}} (\Psi^R + \Psi^L) - |\dot{m}_{i \pm \frac{1}{2}}| (\Psi^R - \Psi^L) \right] + \mathbf{P}_{i \pm \frac{1}{2}}, \quad (36)$$

where

$$\Psi^{L/R} = \begin{bmatrix} 1 \\ u \\ H \end{bmatrix}^{L/R}, \quad \mathbf{P}_{i \pm \frac{1}{2}} = \begin{bmatrix} 0 \\ p_{i \pm \frac{1}{2}} \\ 0 \end{bmatrix}. \quad (37)$$

Here, the superscripts  $L$  and  $R$  indicate the left- and right-side reconstructed values, respectively, on the cell faces in Eqs. (33) and (34);  $p_{i \pm \frac{1}{2}}$  is the pressure applied on the cell face; and  $\dot{m}_{i \pm \frac{1}{2}}$  is the mass flux, which can be obtained as

$$\dot{m}_{i \pm \frac{1}{2}} = (\rho u)_{i \pm \frac{1}{2}} = M_{i \pm \frac{1}{2}} a_{i \pm \frac{1}{2}} \rho_{i \pm \frac{1}{2}}^{L/R}, \quad (38)$$

where  $M_{i \pm \frac{1}{2}}$  is the mean Mach number, and  $a_{i \pm \frac{1}{2}}$  is the mean speed of sound, which can be obtained with simple average as

$$a_{i \pm \frac{1}{2}} = a_{i \pm \frac{1}{2}L}^L + a_{i \pm \frac{1}{2}}^R. \quad (39)$$

In addition,  $\rho_{i \pm \frac{1}{2}}^{L/R}$  is the density of the cell face, which is chosen in an upwind manner, expressed as

$$\rho_{i \pm \frac{1}{2}}^{L/R} = \begin{cases} \rho_{i \pm \frac{1}{2}}^L & \text{if } u_{i \pm \frac{1}{2}} \geq 0, \\ \rho_{i \pm \frac{1}{2}}^R & \text{otherwise.} \end{cases} \quad (40)$$

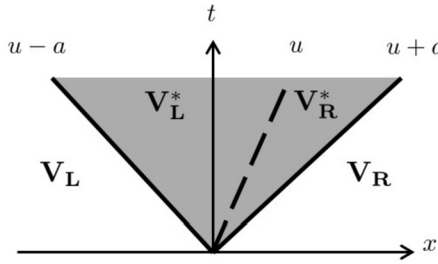


**Fig. 3.** The solution structure of the one-dimensional Riemann problem in the  $x$ ,  $t$ -plane where the “star regions” are marked by the grey area. There are three waves associated with the eigenvalues  $u - a$ ,  $u$  and  $u + a$ .

According to Liou [25], a typical choice to compute  $M_{i\pm\frac{1}{2}}$  in Eq. (38) and  $p_{i\pm\frac{1}{2}}$  in Eq. (37) is to use fourth- and fifth-order polynomials [33], respectively.

Nonetheless, while applying the above scheme to the two-fluid model, undesirable oscillations might be generated on the liquid-gas/gas-liquid interfaces [12,13]. To eliminate these oscillations, Chang and Liou [12] used the exact Riemann solver to successively calculate the flux across the cell face in the different phases. However, as mentioned in Section 1, the required iterations in the Riemann solver consume considerable CPU time. To address this issue, we use the hybrid AUSMD-type Riemann solver, introduced by Niu [13]. In this solver, the PVRS [31] is used to obtain the values of  $\dot{m}_{i\pm\frac{1}{2}}$  in Eq. (38) and  $p_{i\pm\frac{1}{2}}$  in Eq. (37). The corresponding fluxes across the cell faces are then calculated using AUSMD. Moreover, as claimed by Chang and Liou [12], in the stratified flow model, the recognition of the pressure position across the interface is essential to guarantee the momentum balance of a single cell. Therefore, we modify this scheme by relocating the pressure at the cell faces in different phases that share the same cell face [12]. The algorithm of the present hybrid scheme is summarized below.

Starting from the PVRS, the 1D Riemann problem in the primitive variable form can be expressed as

$$\frac{\partial \mathbf{W}}{\partial t} + \mathbf{A} \frac{\partial \mathbf{W}}{\partial x} = 0, \quad (41)$$

where

$$\mathbf{W} = \begin{bmatrix} \rho \\ u \\ p \end{bmatrix}, \quad \mathbf{A} = \begin{bmatrix} u & \rho & 0 \\ 0 & u & 1 \\ 0 & \rho a^2 & u \end{bmatrix}, \quad (42)$$

and the initial condition is

$$\mathbf{W}(x, t=0) = \begin{cases} \mathbf{V}^L & \text{if } x < 0, \\ \mathbf{V}^R & \text{if } x > 0, \end{cases} \quad (43)$$

where  $\mathbf{V}^L$  and  $\mathbf{V}^R$  are two constant states across diaphragm at  $x = 0$ . In Eq. (42), eigenvalues of  $\mathbf{A}$  are

$$\lambda_1 = u - a, \quad \lambda_2 = u, \quad \lambda_3 = u + a. \quad (44)$$

As schematically shown in Fig. 3, the computation domain is divided into four regions by three waves propagating across the domain with speeds,  $u - a$ ,  $u$ , and  $u + a$ , where  $u$ , is a contact discontinuity. Regions that are bounded by lines  $u - a$  and  $u + a$  and separated by the contact discontinuity are usually referred to as the “star region”, in which the velocity  $u^*$  and pressure  $p^*$  are constant, but the density jumps from the left state  $\rho^{*,L}$  to right state  $\rho^{*,R}$  [26]. According to Toro [31], the expressions for  $u^*$ ,  $p^*$ ,  $\rho^{*,L}$  and  $\rho^{*,R}$  in terms of  $\mathbf{V}^L$  and  $\mathbf{V}^R$  are given by

$$p^* = \frac{1}{C^L + C^R} \left[ C^R p^L + C^L p^R + C^L C^R (u^L - u^R) \right], \quad (45)$$

$$u^* = \frac{1}{C^L + C^R} \left[ C^L u^L + C^R u^R + (p^L - p^R) \right], \quad (46)$$

$$\rho^{*,L} = \rho^L + \frac{p^* - p^L}{(a^L)^2}, \quad (47)$$

$$\rho^{*,R} = \rho^R + \frac{p^* - p^R}{(a^R)^2}. \quad (48)$$

While dealing with fluxes across cell faces in the same phases (e.g., gas–gas and liquid–liquid),  $C^L$  and  $C^R$  are obtained with [13,32]

$$C^L = C^R = \bar{\rho}_k \bar{a}_k, \quad (49)$$

where the subscript  $k$  represents either the gas, denoted by  $g$ , or the liquid phase, denoted by  $l$ , and the overbar represents arithmetic means between left- and right-sided constant states ( $\overline{\mathbf{V}}^{L/R}$ ) of the density field  $\rho^{L/R}$  and speed of sound  $a^{L/R}$ . Substituting Eqs. (45)–(48) into Eqs. (36) and (38), the fluxes across the cell face in the same phases  $\mathbf{E}_{k-k}$  can be written as

$$\mathbf{E}_{k-k} = \frac{1}{2} \left[ (\rho_{k-k}^* u_{k-k}^*) (\Psi_k^L + \Psi_k^R) - |\rho_{k-k}^* u_{k-k}^*| (\Psi_k^R + \Psi_k^L) \right] + p^*, \quad (50)$$

where

$$\rho_{k-k}^* = \begin{cases} \rho_{k-k}^{*,L} & \text{if } u_{k-k}^* \geq 0, \\ \rho_{k-k}^{*,R} & \text{if } u_{k-k}^* < 0. \end{cases} \quad (51)$$

For the numerical flux across the cell face in different phase (i.e. liquid–gas),  $C^L$  and  $C^R$  in Eqs. (45) and (46) are chosen to be  $\rho_l^L a_l^L$  and  $\rho_g^R a_g^R$ , respectively, which eliminates large variations in density between different phase due to the arithmetic means. Moreover, as schematically shown in Fig. 1c, because the liquid–gas interface shares the right face of the cell  $i-1$  and the left face of the cell  $i$ , pressure is applied to the liquid phase at the right face of the cell  $i-1$  and to the gas phase at the left face of cell  $i$ . Therefore, the resulting flux on the right face of the cell  $i-1$  can be expressed as

$$\mathbf{E}_{l-g} = \begin{Bmatrix} \max(0, u_{l-g}^*) \rho_{l-g}^* \\ \max(0, u_{l-g}^*) \rho_{l-g}^* u_l^L \\ \max(0, u_{l-g}^*) \rho_{l-g}^* H_l^L \\ \min(0, u_{l-g}^*) \rho_{l-g}^* \\ \min(0, u_{l-g}^*) \rho_{l-g}^* u_g^R \\ \min(0, u_{l-g}^*) \rho_{l-g}^* H_g^R \end{Bmatrix} + \begin{Bmatrix} 0 \\ p^* \\ 0 \\ 0 \\ 0 \\ 0 \end{Bmatrix}, \quad (52)$$

and that on the left face of cell  $i$  can be expressed as

$$\mathbf{E}_{l-g} = \begin{Bmatrix} \max(0, u_{l-g}^*) \rho_{l-g}^* \\ \max(0, u_{l-g}^*) \rho_{l-g}^* u_l^L \\ \max(0, u_{l-g}^*) \rho_{l-g}^* H_l^L \\ \min(0, u_{l-g}^*) \rho_{l-g}^* \\ \min(0, u_{l-g}^*) \rho_{l-g}^* u_g^R \\ \min(0, u_{l-g}^*) \rho_{l-g}^* H_g^R \end{Bmatrix} + \begin{Bmatrix} 0 \\ 0 \\ 0 \\ 0 \\ p^* \\ 0 \end{Bmatrix}. \quad (53)$$

Finally, the formulation of flux across the cell face at the gas–liquid ( $g-l$ ) interface can be derived with the same analogy. Note that not only PVRS but also other approximate Riemann solvers, such as Harten–Lax–van Leer contact (HLLC), can also be used to calculate the mass flux and pressure in the AUSMD algorithm. As no noticeable difference is found between the solutions obtained using PVRS and HLLC, numerical simulations for the examples presented in Section 3 are conducted using the AUSMD scheme incorporated with PVRS only.

## 2.6. Time integration, decoding and update of variables

We apply a forth-order multi-stage Runge-Kutta (RK4) method to the time integration:

$$\mathbf{Q}_k^{(i)} = \mathbf{Q}_k^n + \frac{\Delta t}{4} \mathbf{L}(\mathbf{Q}_k^n), \quad (54)$$

$$\mathbf{Q}_k^{(ii)} = \mathbf{Q}_k^n + \frac{\Delta t}{3} \mathbf{L}(\mathbf{Q}_k^{(1)}), \quad (55)$$

$$\mathbf{Q}_k^{(iii)} = \mathbf{Q}_k^n + \frac{\Delta t}{2} \mathbf{L}(\mathbf{Q}_k^{(2)}), \quad (56)$$

$$\mathbf{Q}_k^{n+1} = \mathbf{Q}_k^n + \Delta t \mathbf{L}(\mathbf{Q}_k^{(3)}), \quad (57)$$

where

$$\mathbf{Q}_k \equiv \begin{bmatrix} Q_k^1 \\ Q_k^2 \\ Q_k^3 \\ Q_k^4 \\ Q_k^5 \end{bmatrix} = \begin{bmatrix} \alpha_k \rho_k \\ \alpha_k \rho_k u_k \\ \alpha_k \rho_k v_k \\ \alpha_k \rho_k w_k \\ \alpha_k \rho_k E_k + p_k^{int} \alpha_k \end{bmatrix}, \quad (58)$$

where superscripts  $n$  and  $n+1$  are the indices for the present and next steps, respectively; (i), (ii), and (iii) indicate the sub-steps in time advancement; and  $L(*)$  indicates the summation of fluxes and nonconservative terms in Eq. (14). The computational time step  $\Delta t$  in Eqs. (54)-(57) is determined by the “Courant–Friedrichs–Levy (CFL) number”, which can be expressed as

$$\text{CFL} = \frac{\Delta t}{\min [\max(a_g, a_l) + \max(|\vec{u}_g|, |\vec{u}_l|)]}. \quad (59)$$

An additional transformation step is required to convert  $\mathbf{Q}_k$  into primitive variables in the next time step. First, the velocity components  $u$ ,  $v$ , and  $w$  for each phase are recovered by

$$u_k = \frac{Q_k^2}{Q_k^1}, \quad v_k = \frac{Q_k^3}{Q_k^1}, \quad w_k = \frac{Q_k^4}{Q_k^1}. \quad (60)$$

Next, the common pressure between different phases is updated by an algebraic equation derived from the stiffened gas EOS as [12–15,22,27,32]

$$p^2 + (-A + B + D)p - AC + BD = 0, \quad (61)$$

where

$$A = (\gamma_g - 1)(Q_g^5 - \Theta_g), \quad (62)$$

$$B = -(\gamma_l - 1)(Q_l^5 - \Theta_l - p) + \gamma_l p_\infty, \quad (63)$$

$$C = \gamma_l p_\infty + (\gamma_l - 1)(p - \delta p^*), \quad (64)$$

$$D = (\gamma_g - 1)(p - \delta p^*), \quad (65)$$

$$\Theta_k = \frac{(Q_k^2)^2 + (Q_k^3)^2 + (Q_k^4)^2}{2Q_k^1}. \quad (66)$$

The solution of pressure  $p$  is the positive root of Eq. (61). The rest of the primitive variables in Eqs. (2) and (3) can be obtained with

$$\alpha_g = \frac{Q_g^5 - \Theta_g}{\frac{p}{\gamma_g - 1} + (p - \delta p^*)}, \quad \alpha_l = 1 - \alpha_g, \quad (67)$$

$$e_k = \frac{1}{Q_k^1} [Q_k^5 - \alpha_k(p - \delta p^*)] - \frac{1}{2}(u_k^2 + v_k^2 + w_k^2), \quad (68)$$

$$T_g = \frac{(\gamma_g - 1)e_g}{R_g}, \quad T_l = \frac{\gamma_l e_l (p + p_\infty)}{C_{p,l}(p + \gamma_l p_\infty)}. \quad (69)$$

However, the ratio between the largest and smallest coefficients in Eq. (61) is very large, because of the involvement of the unrealistically large value of  $p_\infty$  in Eq. (11). Hence, round-off errors can be generated while solving  $p$  and  $\alpha$ . To address this issue, we solve another set of equations derived from the total energy of both fluids in Eq. (58):

$$\begin{cases} F_g = \alpha_g \left( \frac{p}{\gamma_g - 1} + (p^n - \delta p^*) \right) + \Theta_g - Q_g^5 = 0, \\ F_l = (1 - \alpha_g) \left( \frac{p + \gamma_l p_\infty}{\gamma_l - 1} + (p^n - \delta p^*) \right) + \Theta_l - Q_l^5 = 0. \end{cases} \quad (70)$$

In the above equation,  $p^n$  is the known quantity at the current step  $n$ , and the Newton–Raphson iteration is performed to obtain the unknowns  $p$  and  $\alpha_g$ . In our experience, the error of Eq. (70) converges below  $O(10^{-5})$  within 20 iterations.

### 3. Numerical tests

To assess the ability of the present scheme, a series of single-phase and multiphase benchmark tests are conducted in this section. Results from the present hybrid MUSCL-THINC and other existing schemes, such as MUSCL and MUSCL-BVD, are also compared.

### 3.1. Single-phase flows

#### 3.1.1. Advection of complex waves

We consider the transport of complex waves, including discontinuous and smooth profiles, in one dimension. The advection equation for this wave,  $\phi$ , can be written as

$$\frac{\partial \phi}{\partial t} + C_w \frac{\partial \phi}{\partial x} = 0, \quad (71)$$

where  $C_w$  is the constant wave speed, which is set to  $1 \text{ m s}^{-1}$  in this case. Following Jiang and Shu [48], the initial condition is

$$\phi(x) = \begin{cases} \frac{1}{6} [G(x, \beta, z - \delta) + G(x, \beta, z + \delta) + 4G(x, \beta, z)] & |x + 0.7| \leq 0.1, \\ 1 & |x + 0.3| \leq 0.1, \\ 1 - |10(x - 0.1)| & |x - 0.1| \leq 0.1, \\ \frac{1}{6} [F(x, \alpha, a - \delta) + F(x, \alpha, a + \delta) + 4F(x, \alpha, a)] & |x - 0.5| \leq 0.1, \\ 0 & \text{otherwise}, \end{cases} \quad (72)$$

where functions  $G$  and  $F$  are defined as

$$G(x, \beta, z) = \exp \left[ -\beta (x - z)^2 \right] \quad (73)$$

and

$$F(x, \alpha, a) = \sqrt{\max [1 - \alpha^2 (x - a)^2, 0]}, \quad (74)$$

respectively, and the coefficients,  $\alpha$ ,  $\beta$ ,  $a$ ,  $z$ , and  $\delta$  are

$$\alpha = 10, \beta = \frac{\log 2}{36\delta^2}, a = 0.5, z = -0.7, \delta = 0.01. \quad (75)$$

Four cases with different resolutions, 200, 400, 600, and 800 mesh points, are simulated. Both MUSCL [33] and hybrid MUSCL-THINC schemes are applied to these cases, and the parameter  $\beta$  in Eq. (25), which controls the sharpness of the hyperbolic tangent function, is set to 1.8 in the hybrid MUSCL-THINC scheme. The periodic boundary condition is imposed at both ends of the computational domain. This case is commonly used to evaluate the non-oscillatory property and numerical diffusion of the discontinuity-sharpening schemes (see [37,38,40]). Numerical results at  $t = 2.0$  s using the MUSCL (black lines) and hybrid MUSCL-THINC (red dashed lines) schemes with different resolutions along with exact solutions (gray lines) are plotted in Fig. 4. It can be seen that although the MUSCL scheme with TVD limiter (minmod) is able to prevent numerical oscillations near the discontinuities, it is too diffusive to well resolve the complex wave forms even if we increase the grid resolution up to 800 cells (see Fig. 4d). On the other hand, by combining MUSCL and THINC, the proposed hybrid scheme significantly suppresses the numerical diffusion. The reason is that due to the weighted parameter,  $\zeta$ , in Eq. (35) the sharpness at the cell can be effectively detected so that the hybrid MUSCL-THINC scheme is enforced to behave like THINC when  $\zeta \rightarrow 1$  (see Eqs. (33) and (34)). Thus, jumps of local profiles can be captured properly by the proposed hybrid scheme.

#### 3.1.2. Shock tube problems

These are problems when two constant fluid states are initially separated by a diaphragm located at the center of the domain. The problem is normally used to test the scheme's capability of resolving the shock waves and moving discontinuities [49]. In the first problem, the initial conditions are listed in Table 2. Here, computations are conducted using 200 cells. Both MUSCL and hybrid MUSCL-THINC schemes are used, and  $\beta$  in the present hybrid MUSCL-THINC scheme is set to 2.0. Profiles of the pressure and density at  $t = 0.25$  s along with the exact solutions [26] are presented in Fig. 5. It can be seen that the present scheme captures both continuous and discontinuous profiles without excessive numerical oscillation and diffusion. Comparison of results from the MUSCL and hybrid MUSCL-THINC schemes demonstrates that the present scheme gives less numerical diffusion near the discontinuities in both the pressure (Fig. 5a) and density (Fig. 5b) profiles.

To further test the capability of the proposed scheme, in the second problem, we change the initial conditions, as summarized in Table 3, and perform the same calculation. The solution profiles of the pressure and density at  $t = 0.16$  s along with the exact solutions [26] are shown in Figs. 6a and b, respectively. Again, it shows that, compared with the MUSCL scheme, the proposed scheme reduces the numerical diffusion more effectively, and the discontinuities can be better captured.

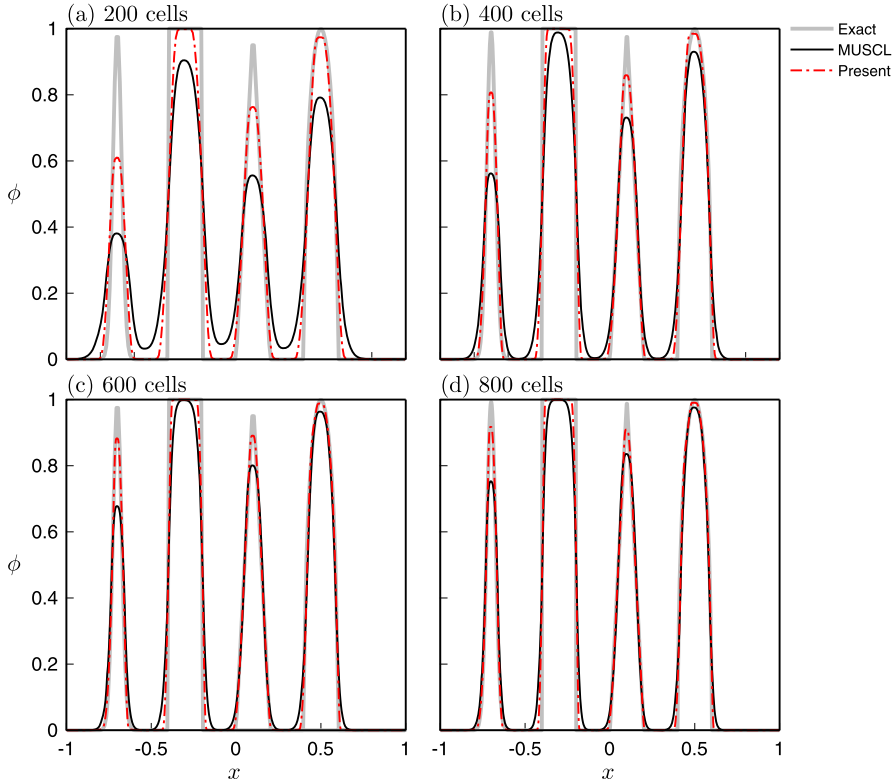


**Fig. 4.** Numerical results from the advection of complex waves at  $t = 2$  s with the initial conditions given by Eq. (72) using (a) 200, (b) 400, (c) 600, and (d) 800 grid cells. The gray lines represent exact solutions. The black lines represent the numerical solutions obtained using MUSCL, and the red dashed lines represent the solutions obtained using the hybrid MUSCL-THINC scheme. (For interpretation of the colors in the figure(s), the reader is referred to the web version of this article.)

**Table 2**  
Initial conditions for the first shock tube problem.

	Left states	Right states	Units
$p$	1	0.1	Pa
$u$	0	0	$\text{m s}^{-1}$
$\rho$	1	0.13	$\text{kg m}^{-3}$

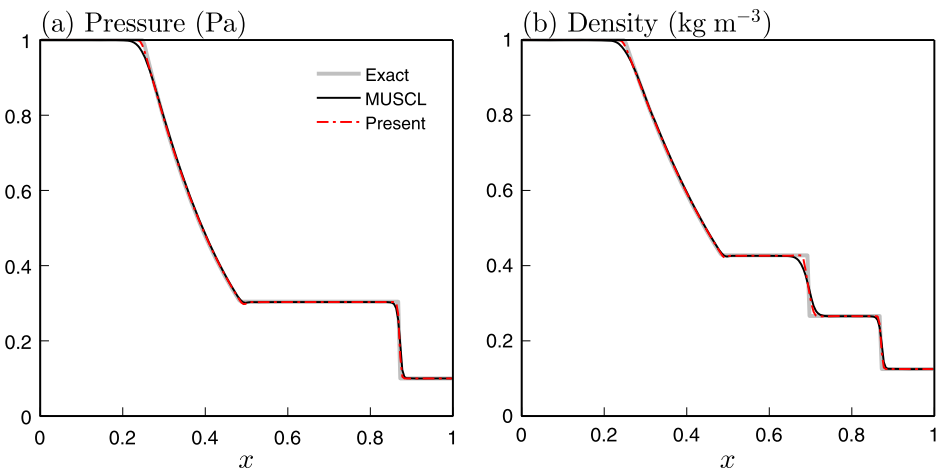


**Fig. 5.** State profiles for the shock tube problem at  $t = 0.25$  s with the initial conditions listed in Table 2. The gray lines represent the exact solutions [26]. The black lines represent solutions obtained by the MUSCL scheme, and red dashed lines are solutions obtained from the hybrid MUSCL-THINC scheme.

**Table 3**  
Initial conditions for the second shock tube problem.

	Left states	Right states	Units
$p$	3.53	0.57	Pa
$u$	0.70	0	$\text{m s}^{-1}$
$\rho$	0.45	0.5	$\text{kg m}^{-3}$

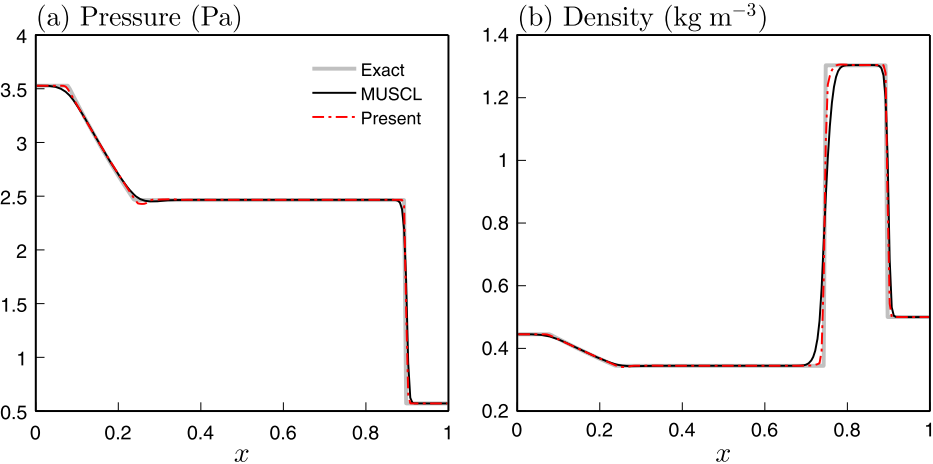


**Fig. 6.** State profiles for the shock tube problem at  $t = 0.25$  s with the initial conditions listed in Table 3. The gray lines represent the exact solutions [26]. The black lines represent solutions obtained by the MUSCL scheme, and red dashed lines are solutions obtained by the hybrid MUSCL-THINC scheme.

### 3.1.3. Two interacting blast waves

Here, we perform the test case of the interaction between two blast waves, following Woodward and Colella [50]. The problem starts from prescribing three constant initial states in a gas flow. Then two strong blast waves develop and collide with each other as time evolves. This produces multiple interactions between strong shocks and rarefaction waves, which are regarded as a challenging problem for shock capturing schemes because peaks of the density distribution need to be well resolved. In this problem, initial distributions of density, velocity and pressure are given by

$$(\rho, u, p) = \begin{cases} (1000, 0, 1) & 0 \leq x \leq 0.1, \\ (0.01, 0, 1) & 0.1 < x \leq 0.9, \\ (100, 0, 1) & 0.9 < x \leq 1.0. \end{cases} \quad (76)$$

Cases with four different resolutions using 400, 600, 800 and 6400 mesh points, are conducted. The case with the finest resolution using MUSCL is used as the reference, while both MUSCL and hybrid MUSCL-THINC schemes are applied to all the other cases. Here,  $\beta$  in the hybrid MUSCL-THINC scheme is set to 1.6. The reflective boundary condition is imposed at both ends of the computational domain. We set  $\Delta t / \Delta x = 0.01$ , which maintains the numerical stability. Results of density profiles at  $t = 0.04$  s using the MUSCL and hybrid MUSCL-THINC schemes with various resolutions along with the reference solutions are presented in Fig. 7. Again, it can be seen that the present hybrid MUSCL-THINC scheme can capture the sharp density jump more effectively than MUSCL. The difference between the two can be significant in cases of the coarser grid resolution (see Figs. 7a and b). In particular, because MUSCL tends to smear discontinuities of the density, the density distribution along contact discontinuity (i.e.,  $x \simeq 0.6$ ) can be better resolved using less mesh points by the present hybrid MUSCL-THINC scheme. Fig. 7 also shows that no significant difference between the results from the present hybrid scheme and reference solution is found when the number of mesh points  $\leq 600$  (see Figs. 7b and c), demonstrating the effectiveness of the present hybrid scheme in capturing sharp discontinuities.

### 3.1.4. Double Mach reflection

In this section, following Woodward and Colella [50], a hypersonic planar shock wave propagating with Mach number ( $M$ ) = 10 reflected by a  $30^\circ$  ramp is simulated. The initial conditions of state variables are summarized in Table 4. As shown in Fig. 8, computations are performed in a domain with dimensions  $L_x \times L_y = 4 \text{ m} \times 1 \text{ m}$  using the grid resolution of  $N_x \times N_y = 1000 \times 250$ , for which  $x$  and  $y$  denote the streamwise and vertical directions, respectively. A right moving shock wave with an inclined angle,  $60^\circ$ , relative to  $x$ -axis is imposed, which simulates a normal shock wave impinging a  $30^\circ$  ramp. The inlet and outlet boundary conditions are imposed at the left and right boundaries, respectively. At the bottom boundary, two types of the boundary condition are imposed. In the region behind the shock wave (e.g.,  $x = 0\text{--}1/6$  in Fig. 8),

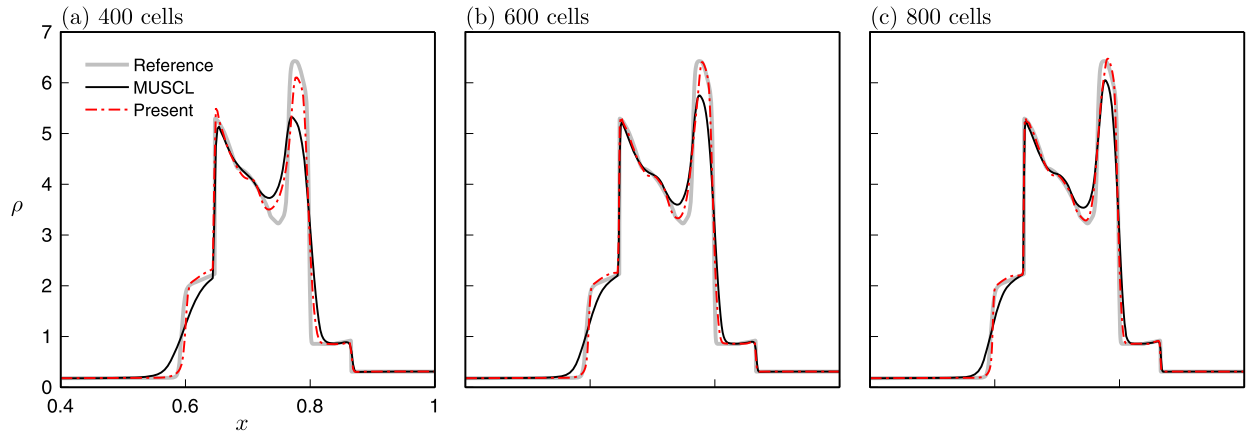


**Fig. 7.** Zoom-in density profiles in the case of two interacting blast waves at  $t = 0.04$  s with the initial conditions given by Eq. (76) using (a) 400, (b) 600, and (c) 800 mesh points. The gray lines represent the reference solutions. The black lines represent the solutions obtained by the MUSCL scheme, and the red dashed lines represent the solutions obtained by the present hybrid MUSCL-THINC scheme.

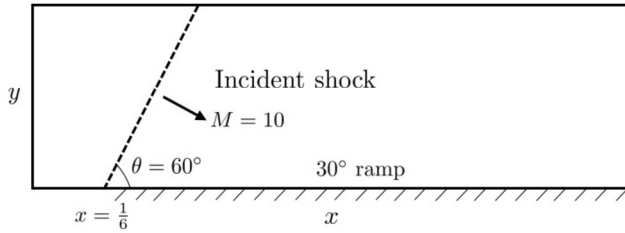


**Fig. 8.** Domain configuration for the test of double Mach reflection along with the initial position of the incident shock wave (black dashed line).

**Table 4**  
Initial conditions for the problem of double Mach reflection.

	Behind the shock	In front of the shock	Units
$p$	116.5	1	Pa
$u$	$8.25 \times \cos(30^\circ)$	0	$\text{m s}^{-1}$
$v$	$-8.25 \times \sin(30^\circ)$	0	$\text{m s}^{-1}$
$\rho$	8.0	1.4	$\text{kg m}^{-3}$

values behind the shock listed in Table 4 are assigned. Otherwise, the reflective wall boundary condition is imposed. At the top boundary, values behind and in front of the shock wave in Table 4 are imposed according to the location of the shock wave moving along the top boundary at each time step. The computational time step ( $\Delta t$ ) is set to  $2 \times 10^{-5}$  s. Both MUSCL and hybrid MUSCL-THINC schemes are tested in this example. To evaluate the sensitivity to the coefficient  $\beta$  (see Eq. (25)),  $\beta = 2.4$  and  $3.0$ , are used in the present hybrid MUSCL-THINC scheme.

Density contours of  $\rho$  ranging from 19 to 21 from the numerical results at  $t = 0.2$  s and the corresponding enlarged views in the recirculation zone are presented in Fig. 9. It can be seen that in general, shock waves corresponding to density jumps in Fig. 9 obtained by the hybrid MUSCL-THINC scheme (Figs. 9a and b) have more compact thickening than those obtained by the MUSCL scheme, indicating that the present hybrid scheme effectively reduces the numerical diffusion. Moreover, comparison between Figs. 9b and c shows that, as  $\beta$  increases, more details of flow structures, such as those vortices resulting from the Kelvin-Helmholtz instability at the bottom of the domain (slip line), can be produced (see the zoom-in snapshots in Fig. 9c). Those structures are usually treated as indicators to verify the performance of the reconstruction schemes [38–40,51]. Fig. 9 indicates that the present hybrid scheme with the higher  $\beta$  values is capable of resolving the shock waves and the associated complex flow structures effectively and results in less numerical diffusion compared with the MUSCL scheme.

It should be noted that the jet along the lower wall in Fig. 9 is slightly suffered from the so called “carbuncle phenomenon” due to the Riemann solver [52]. Various treatments for seeking solutions to cure such an issue are provided in the recent literatures (e.g., [53–55]), but those are beyond the scope of the current research. This study only aims to show that the proposed scheme has capability of resolving both discontinuities and smooth solutions in two-phase flow modeling.

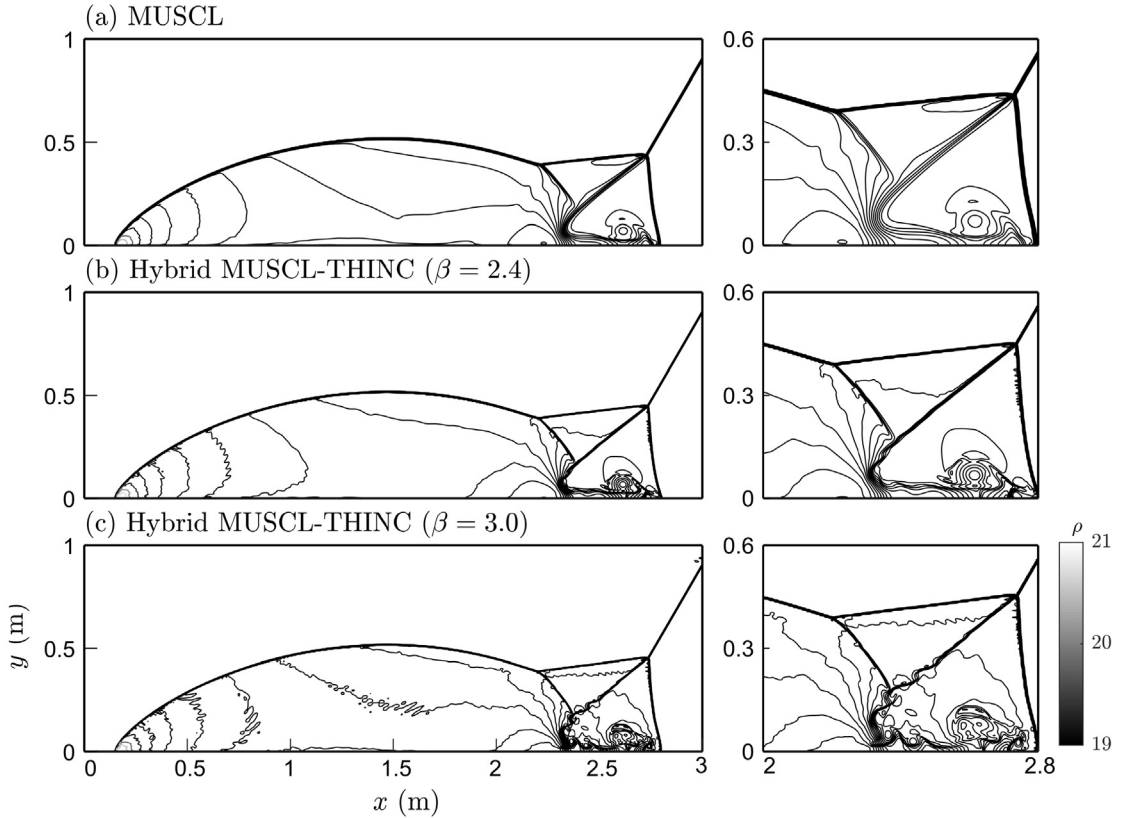


**Fig. 9.** Density contours obtained by (a) MUSCL, (b) Hybrid MUSCL-THINC with  $\beta = 2.4$ , and (c) Hybrid MUSCL-THINC with  $\beta = 3.0$  for the problem of double Mach reflection at  $t = 0.2$  s with the initial condition listed in Table 4. The right column is the zoom-in snapshots in the recirculation zone.

**Table 5**

Initial conditions for the gas-to-liquid shock tube problem. The subscript  $k$  represents either the gas, denoted by  $g$ , or the liquid phase, denoted by  $l$ , and  $\epsilon = 1 \times 10^{-7}$ .

	Left states	Right states	Units
$\alpha_g$	$1 - \epsilon$	$\epsilon$	
$p$	$10^9$	$10^5$	Pa
$u_k$	0	0	$m s^{-1}$
$T_k$	308.15	308.15	K

### 3.2. Two-phase flows

#### 3.2.1. Gas-to-liquid shock tube problem

We consider a 1D gas-to-liquid shock tube problem where two constant fluid states are separated by a diaphragm located at the domain center. The initial conditions are listed in Table 5, which is the same as those used in the benchmark test conducted in Pailhère et al. [21].

Two cases with different resolutions using 5000 and 500 mesh points are conducted, and the case with the finer resolution is used as the reference. Both MUSCL and hybrid MUSCL-THINC schemes are applied to the coarse-resolution case, whereas the MUSCL scheme is applied to the fine-resolution case. The parameter  $\beta$  in Eq. (25), which controls the sharpness of the hyperbolic tangent function, is set to 2.0 in the hybrid MUSCL-THINC scheme. This case is conducted to demonstrate that the hybrid MUSCL-THINC scheme can dynamically adjust the dominance between MUSCL and THINC. That is, if a smooth profile is obtained, the proposed hybrid scheme acts as MUSCL. Otherwise, the scheme behaves like THINC.

Fig. 10 shows profiles of solutions along with an enlarged view of the particular position at which the discontinuities are present. As shown in Fig. 10b, the high pressure difference at the gas–liquid interface induces a strong shock wave transmitted into the liquid side and a rarefaction fan traveling back into the air. Because the speed of sound in liquid is much higher than that in air, the shock wave moves faster than the rarefaction fan, as shown in Figs. 10b and c. The hybrid MUSCL-THINC scheme is found to retain the sharp discontinuities, including the shock wave and interface (see Fig. 10a), and yield solutions that are much closer to the reference case than the MUSCL-only case.

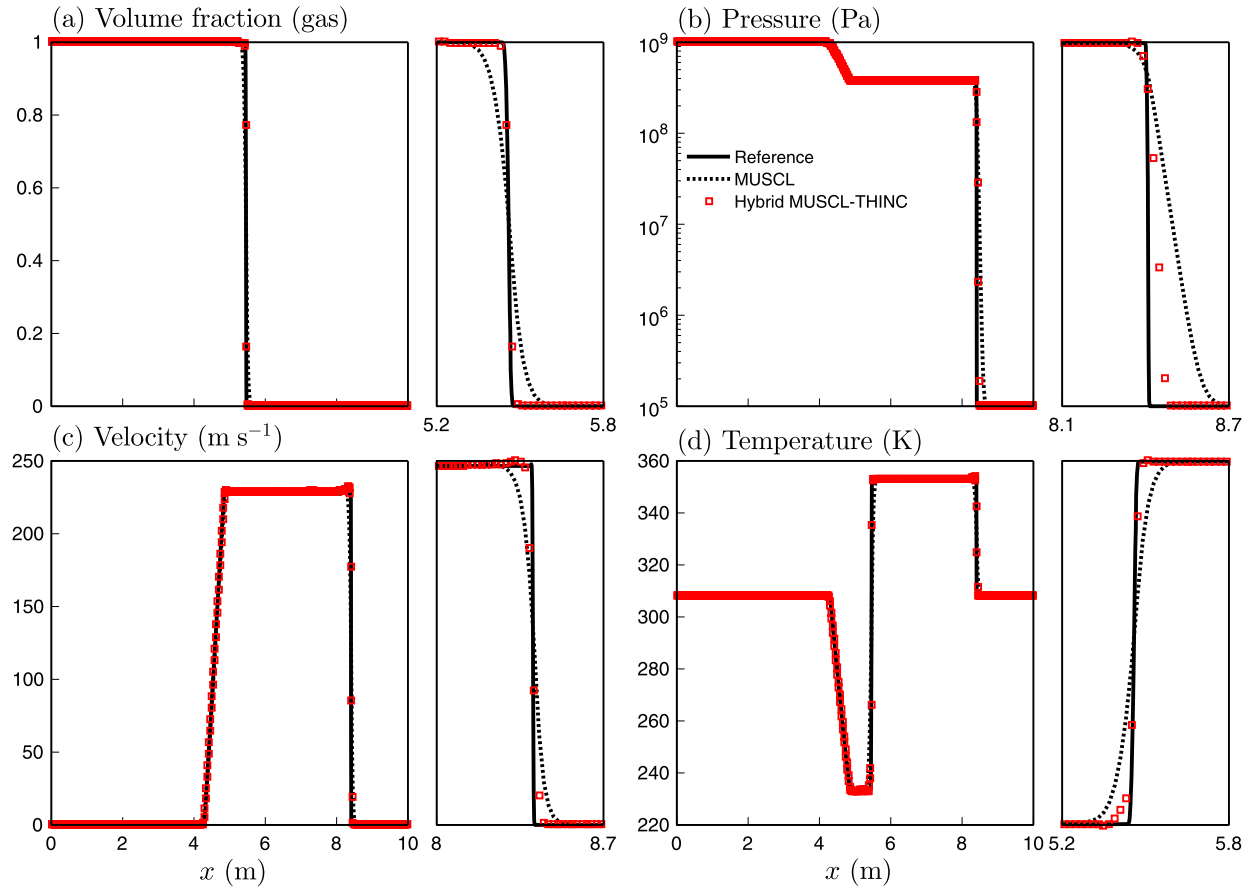


**Fig. 10.** State profiles for the gas-to-liquid shock tube problem with enlarged views at discontinuities using the initial conditions listed in Table 5.

**Table 6**

Initial conditions for the liquid-to-gas shock tube problem. The subscript  $k$  represents either the gas, denoted by  $g$ , or the liquid phase, denoted by  $l$ , and  $\epsilon = 1 \times 10^{-7}$ .

	Left states	Right states	Units
$\alpha_g$	$\epsilon$	$1 - \epsilon$	
$p$	$10^7$	$5 \times 10^6$	Pa
$u_k$	0	0	$m s^{-1}$
$T_k$	308.15	308.15	K

Fig. 11 presents the profiles of the volume fraction using hybrid MUSCL-THINC and the THINC scheme. It can be seen that both the present and THINC schemes give results which are fairly close to the reference solutions. However, the THINC scheme performs slightly better in that, as shown by the markers along the jumps in Fig. 11, the present scheme needs about six grid points to resolve interface, as opposed to two to three grid points in the THINC-only case. This is due to the fact that, while MUSCL is incorporated with the present hybrid scheme, the associated diffusive property cannot be completely eliminated even though an infinitesimal value is imposed for  $\zeta$ . In fact, the present hybrid MUSCL-THINC scheme is suitable for variables comprising both smooth and discontinuous profiles but can be less superior than THINC when dealing with the variables that only comprise jump discontinuities, such as the volume fraction. Therefore, as emphasized in the flow chart in Fig. 2, in our simulation, we use only THINC for the calculation of the volume fraction to avoid numerical diffusion.

### 3.2.2. liquid-to-gas shock tube problems

In this numerical test, we change the initial conditions of the previous problem in Section 3.2.1 in the way that the left half of the domain is occupied by liquid, whereas the right half of the domain is occupied by gas. Initial conditions are listed in Table 6, and the simulation setup is the same as that presented in Section 3.2.1.

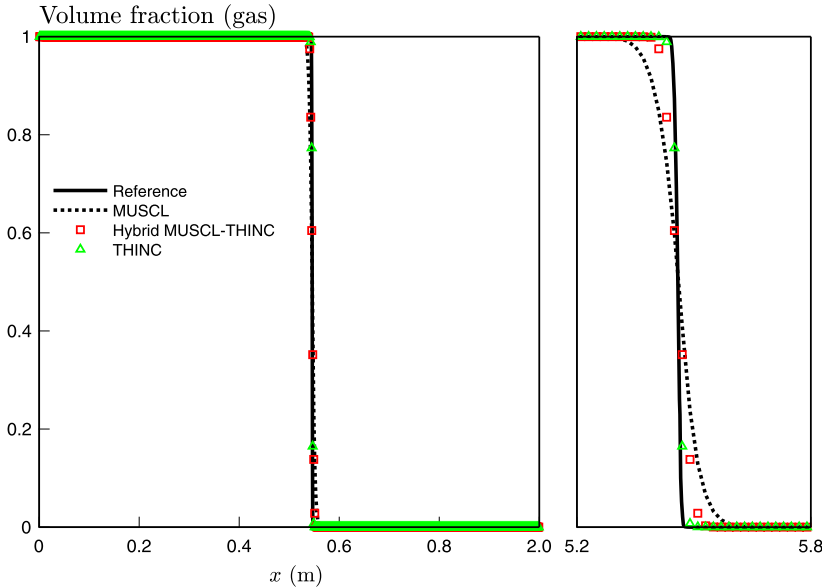


**Fig. 11.** Profiles of volume fraction for the gas-to-liquid shock tube with the initial conditions listed in Table 5 using the hybrid MUSCL-THINC (red squares), THINC (green triangles), and MUSCL (dotted line) schemes along with the reference solution. The right panel is a zoom-in plot at the jump.

**Table 7**

Initial conditions for liquid-to-gas shock tube problem with a high pressure ratio. The subscript  $k$  represents either the gas, denoted by  $g$ , or the liquid phase, denoted by  $l$ , and  $\epsilon = 1 \times 10^{-5}$ .

	Left states	Right states	Units
$\alpha_g$	$\epsilon$	$1 - \epsilon$	
$p$	$10^8$	$10^5$	Pa
$u_k$	0	0	$m s^{-1}$
$T_k$	308.15	308.15	K

**Table 8**

Initial conditions for the problem of Air/R22 shock bubble interaction. Here, the subscript  $k$  stands for either the R22 or gas phase, and  $\epsilon = 1 \times 10^{-5}$ .

	Behind the shock	Before the shock	Inside the bubble	Units
$\alpha_g$	$1 - \epsilon$	$1 - \epsilon$	$\epsilon$	
$p$	$1.59 \times 10^5$	$1.01 \times 10^5$	$1.01 \times 10^5$	Pa
$u_k$	-113.5	0	0	$m s^{-1}$
$v_k$	0	0	0	$m s^{-1}$
$T_k$	328.6	288.2	288.2	K

Fig. 12 shows solution profiles along with the enlarged views at the locations where the discontinuities are present. Due to the lower compressibility of liquid, it is difficult for shock waves to transmit from the liquid into the gas. Hence, only a shock wave with a small amplitude is observed at  $x \approx 5.70$  m, and a strong rarefaction fan is generated at the interface and transmitted back to the liquid, as shown in Fig. 12b. It can be seen that, compared with MUSCL, the hybrid MUSCL-THINC scheme provides more accurate solution profiles and retains sharper gradient at the discontinuity without generating spurious oscillations. In addition, the present hybrid method is further extended to a liquid-to-gas shock tube with a high pressure ratio by applying the initial conditions summarized in Table 7, and the results are presented in Fig. 13. Similar to the previous results, Fig. 13b shows a weak shock wave and steep rarefaction fan on the air and water sides, respectively. Fig. 13 also shows that the hybrid scheme resolves the discontinuities better than the MUSCL scheme. Thus far, we have shown that the present hybrid AUSMD flux algorithm along with the hybrid MUSCL-THINC sharpening method is robust and can give accurate results. Next, two-dimensional (2D) cases are further tested to demonstrate the robustness of the scheme.

### 3.2.3. Air/R22 shock bubble interaction

We consider a shock wave in the air impinging on a stationary R22 refrigerant bubble/column with diameter 50 mm, which is a classical 2D test conducted for the performance evaluation [41,42,56]. Following Nonomura et al. [56], the initial-state variables are set as summarized in Table 8.

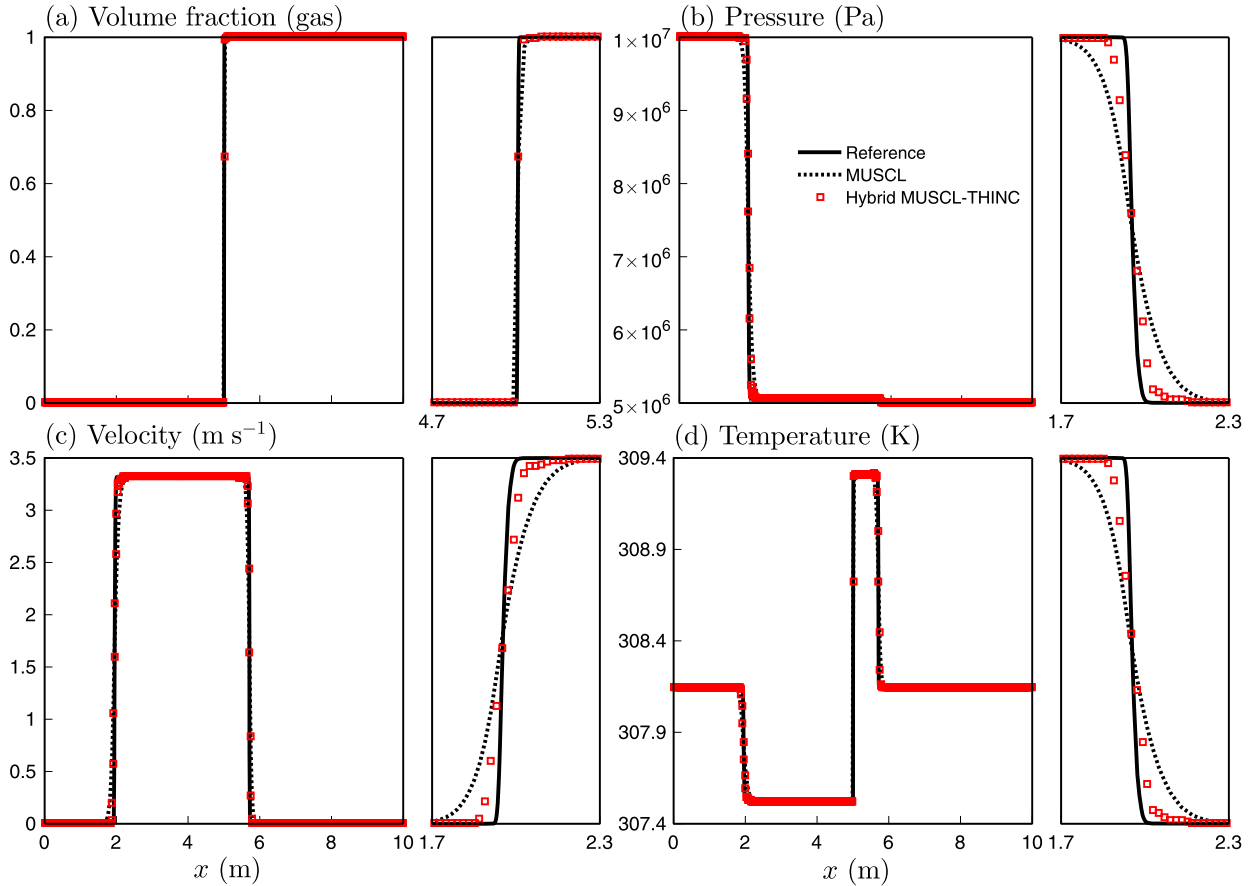


**Fig. 12.** State profiles for the liquid-to-gas shock tube with enlarged views at discontinuities. The initial conditions are listed in Table 6.

As shown in Fig. 14, computations are performed in a domain with dimensions  $L_x \times L_y = 0.45 \text{ m} \times 0.09 \text{ m}$  by using a grid resolution of  $N_x \times N_y = 3560 \times 356$ . In addition,  $x$  and  $y$  denote the streamwise and vertical directions of the domain, respectively, and the R22 bubble is located at the domain center. A left-moving shock wave with  $M = 1.22$  is set at  $x = 0.25 \text{ m}$ . The inlet and outlet conditions are imposed at the left and right boundaries, respectively, and the reflective wall condition is imposed at both the top and bottom boundaries. The computational time step ( $\Delta t$ ) is fixed such that the CFL number = 0.5 throughout the simulation. Three different schemes are used for reconstructing the state variables: MUSCL, scheme proposed by Nonomura et al. [56], who used THINC for determining the volume fraction and MUSCL for determining the other variables, and the proposed hybrid MUSCL-THINC scheme with  $\beta = 2.0$  (Eqs. (33) and (34)). Schlieren-type images of the density gradient and volume fraction of R22 for these schemes are compared in Fig. 15.

As shown in Figs. 15a-c, when the left-moving shock wave hits the R22 bubble, its speed decreases after transmission and a reflective shock wave is generated due to the mismatch of the acoustic impedance (i.e.,  $\rho_k a_k$  between fluid interface [57]). As shown in Figs. 15d-f, once the transmitted shock wave arrives at the downstream pole of the R22 bubble, it collides with the diffracted shock wave due to the convergent geometry, leading to shock focusing and formation of a secondary shock wave. Moreover, Figs. 15g-o show that while all shock waves pass over the R22 bubble, baroclinic vorticity deposits locally at the R22 interface because of the misalignment of the pressure and density gradients. This results in the formation of a vortex pair at the diametral plane, which is similar to the mechanism of Richtmyer-Meshkov instability [58,59]. A comparison between the first and second columns in Fig. 15 shows that the second column better resolves the sharp interface, as the thickening in the first column can be substantially reduced. Besides this difference, the flow features appear to be relatively similar between the two cases. This reflects the fact that even though Nonomura et al. [56] applied THINC to the volume fraction to limit the interface thickening, the other state variables were still obtained using MUSCL. Thus, similar to the original MUSCL scheme, diffusion may still occur near a sharp gradient in different variable fields. In contrast, a comparison between the second and third columns in Fig. 15 shows that the proposed hybrid MUSCL-THINC scheme retains not only the interface sharpness but also more detailed flow features. For example, the billows generated along the interface due to the shear instability and the breakup of small fragments into the air because of the inertia of the shock wave can only be observed in Figs. 15i, j, and o.

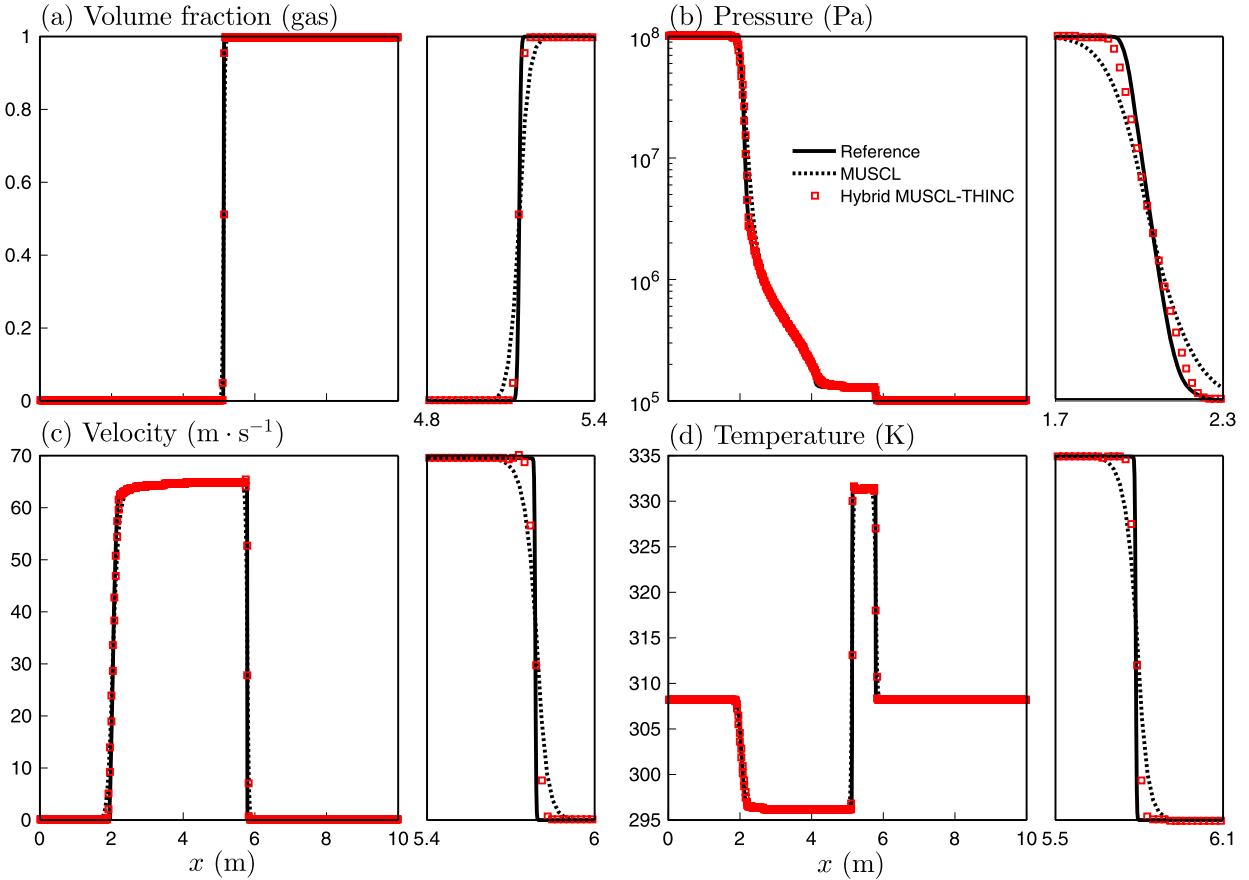


**Fig. 13.** State profiles for the high-pressure-ratio liquid-to-gas shock tube problem with enlarged views at discontinuities. The initial conditions are given in Table 7.

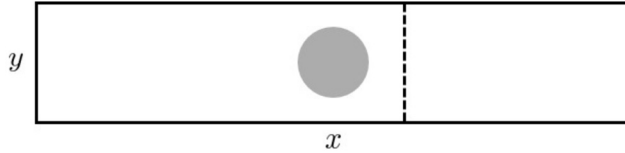


**Fig. 14.** Domain configuration of either air/R22 shock bubble interaction (Sec. 3.2.3) or air/Helium shock bubble interaction (Sec. 3.2.4). The grey circle represents the bubble in these two cases. Here,  $x$  and  $y$  denote the streamwise and vertical directions, respectively. The dimension of the domain is given by  $L_x \times L_y = 0.45 \text{ m} \times 0.09 \text{ m}$ . The dashed line represents a left-moving shock originally located at  $x = 0.25 \text{ m}$  in the case of air/R22 shock bubble interaction or  $x = 0.28 \text{ m}$  in the case of air/Helium shock bubble interaction.

We also implement the MUSCL-THINC BVD scheme proposed by Deng et al. [41] in this case and compare the results with the present scheme using various values of  $\beta$  ranging from 1.6 to 2.0, which are shown in Fig. 16. It is found that as  $\beta$  increases, more details of flow structures (i.e., Kelvin-Helmholtz billows) can be produced (see Figs. 16a-c and d-f). Furthermore, although there exist several differences in the flow pattern, numerical results obtained by the hybrid MUSCL-THINC scheme are relatively similar to those obtained using MUSCL-THINC BVD scheme [41].

### 3.2.4. Air/Helium shock bubble interaction

Another well-known two-dimensional benchmark test, where a shock wave in the air impinges on a Helium bubble/column with the diameter of 50 mm, is considered. The computational domain is the same as that used in Section 3.2.3 (see Fig. 14). The inlet and outlet conditions are imposed at the left and right end boundary, respectively, and the reflective wall boundary condition is imposed at both top and bottom boundaries. As summarized in Table 9, we set the initial conditions following Pandare et al. [28] and Cheng et al. [43]. The computational time step ( $\Delta t$ ) is fixed such that the CFL number = 0.5 throughout the simulation. Three different schemes are used for the reconstruction of the state variables, which are MUSCL,

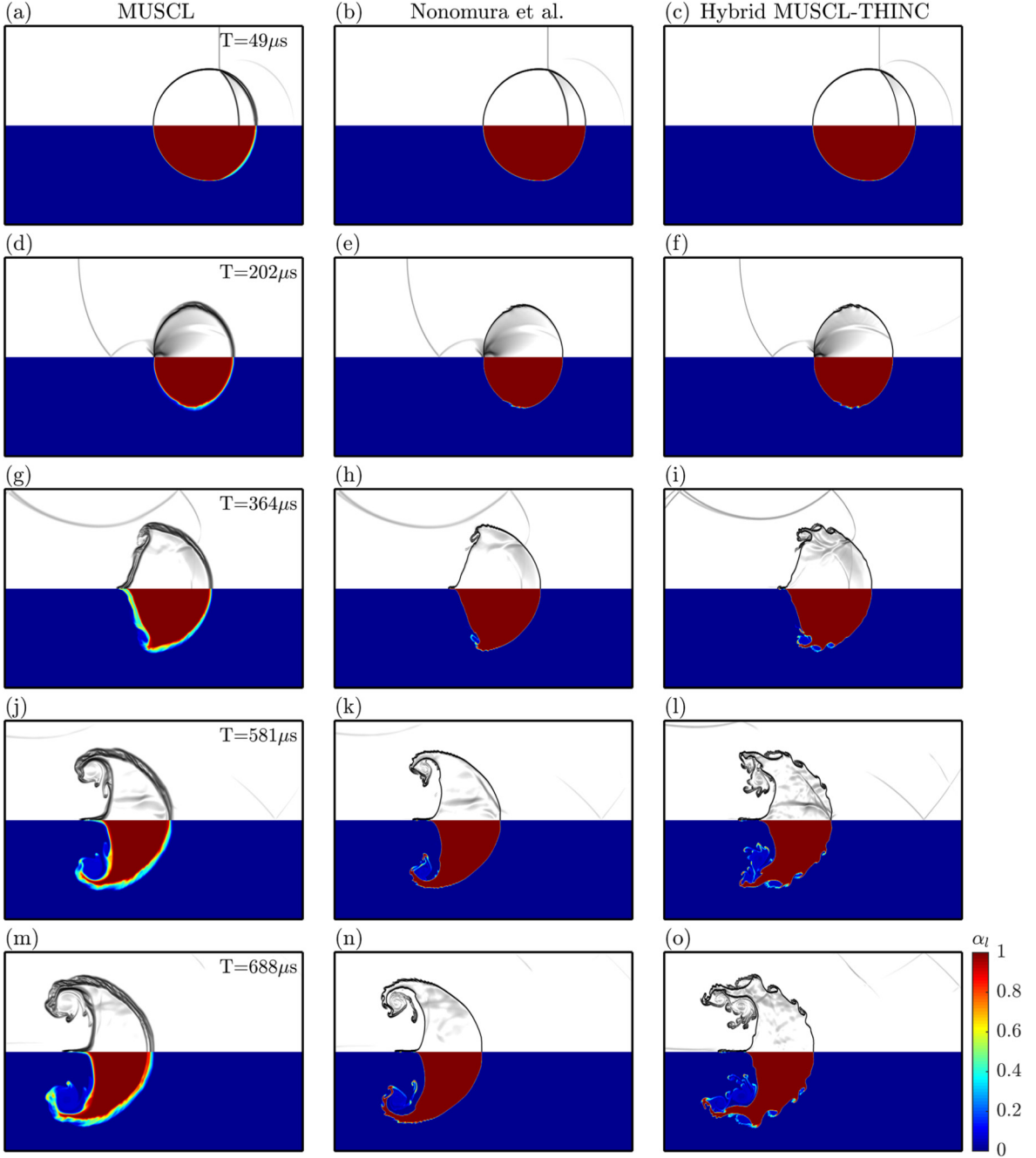


**Fig. 15.** Zoom-in snapshots of the Air/R22 shock bubble interaction obtained by different reconstruction schemes at representative time instants under the initial condition listed in Table 8. The first column presents results from MUSCL reconstruction, the second column is from Nonomura et al. [56], and the third column is from the proposed hybrid MUSCL-THINC scheme. The upper part in each sub-figure is the numerical Schlieren function of the density gradient, while the lower part is the volume fraction of the R22 refrigerant.

MUSCL-THINC BVD scheme proposed by Deng et al. [41] with  $\beta = 1.6$ , and the present hybrid MUSCL-THINC scheme with  $\beta = 1.6$ . The simulation begins with a left-moving shock wave with  $M = 1.22$  initially located at  $x = 0.28$  m (see Fig. 14).

The Schlieren-type image of the density gradient and the volume fraction of Helium obtained using different schemes are presented in Fig. 17. The first column in Fig. 17 shows that MUSCL scheme suffers from severe numerical diffusion such that the material interface tends to be smeared in the earlier stage of simulation. On the other hand, both MUSCL-THINC BVD and the present schemes maintain the compact thickening of material interfaces (see the second and third columns in Fig. 17). Moreover, the small-scale vortices due to the baroclinic effect are clearly produced by both the MUSCL-THINC BVD

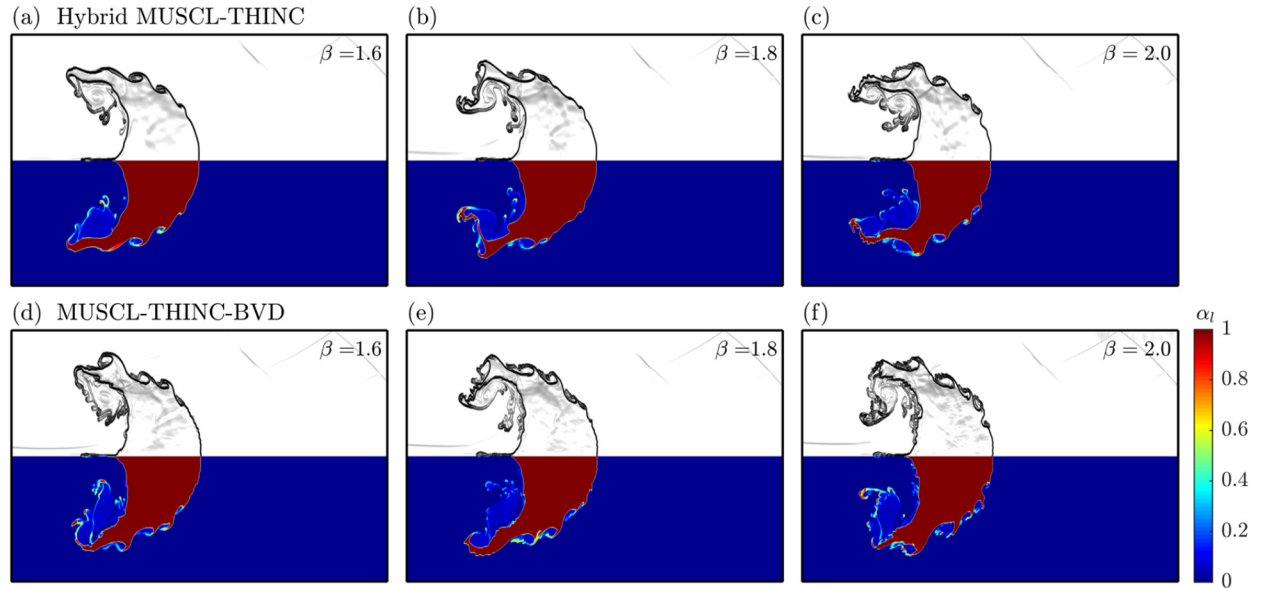


**Fig. 16.** Zoom-in snapshots of the Air/R22 shock bubble interaction obtained by hybrid MUSCL-THINC (upper half) and MUSCL-THINC BVD (lower half) at  $t = 688 \mu\text{s}$  along with different values of  $\beta$  ranging from 1.6 to 2.0. The upper part in each sub-figure is the numerical Schlieren function of the density gradient, while the lower part is the volume fraction of the R22 refrigerant.

**Table 9**

Initial conditions for the problem of Air/Heilium shock bubble interaction. Here, the subscript  $k$  stands for either the Helium or gas phase, and  $\epsilon = 1 \times 10^{-5}$ .

	Behind the shock	Before the shock	Inside the bubble	Units
$\alpha_g$	$1 - \epsilon$	$1 - \epsilon$	$\epsilon$	
$p$	$1.57 \times 10^5$	$1.01 \times 10^5$	$1.01 \times 10^5$	Pa
$u_k$	-113.5	0	0	$\text{m s}^{-1}$
$v_k$	0	0	0	$\text{m s}^{-1}$
$T_k$	283.86	248.88	248.88	K

**Table 10**

CPU times for Air/R22 and Air/Heilium shock bubble interactions reconstructed by MUSCL, hybrid MUSCL-THINC and MUSCL-THINC BVD schemes.

Case	MUSCL	Hybrid MUSCL-THINC	MUSCL-THINC BVD
Air/R22 shock bubble interaction	80227 s	99725 s	198987 s
Air/Heilium shock bubble interaction	67333 s	73652 s	139549 s

and the present schemes, whereas the material interface obtained by MUSCL is so diffusive that these small-scale vortices can not be seen.

In Table 10, we list the CPU times for Air/R22 (Section 3.2.3) and Air/Heilium (Section 3.2.4) shock bubble interactions reconstructed by MUSCL, hybrid MUSCL-THINC and MUSCL-THINC BVD schemes. The CPU used to conduct these simulations is Intel Xeon Silver 4110 (2.1 GHz) with single processor. It can be found from Table 10 that with our implementation for these two examples, the MUSCL-THINC BVD scheme takes about two times longer than MUSCL, while the present hybrid MUSCL-THINC scheme takes only 1.1–1.25 times longer than MUSCL. This shows that the present scheme is able to retain the high computational efficiency but still maintains the sharpness of material interfaces and associated wave patterns. It should be noted that, while computational time varies depending on different computational facilities, Table 10 merely provides a simple reference for comparison between different schemes based on our computational resources and implementation.

### 3.2.5. Water shock air bubble interaction

Test on the water-shock air bubble interaction in a high pressure ratio ( $\sim 0(10^4)$ ) [12,15,22,28,56] is presented in this section. In this case, computations are conducted in a domain with dimensions  $L_x \times L_y = 0.03 \text{ m} \times 0.03 \text{ m}$  by using grid resolution of  $N_x \times N_y = 1000 \times 1000$ , and initial conditions are given in Table 11. Inlet and outlet conditions are imposed at the left and right boundaries, respectively, and the open boundary condition is imposed at both the top

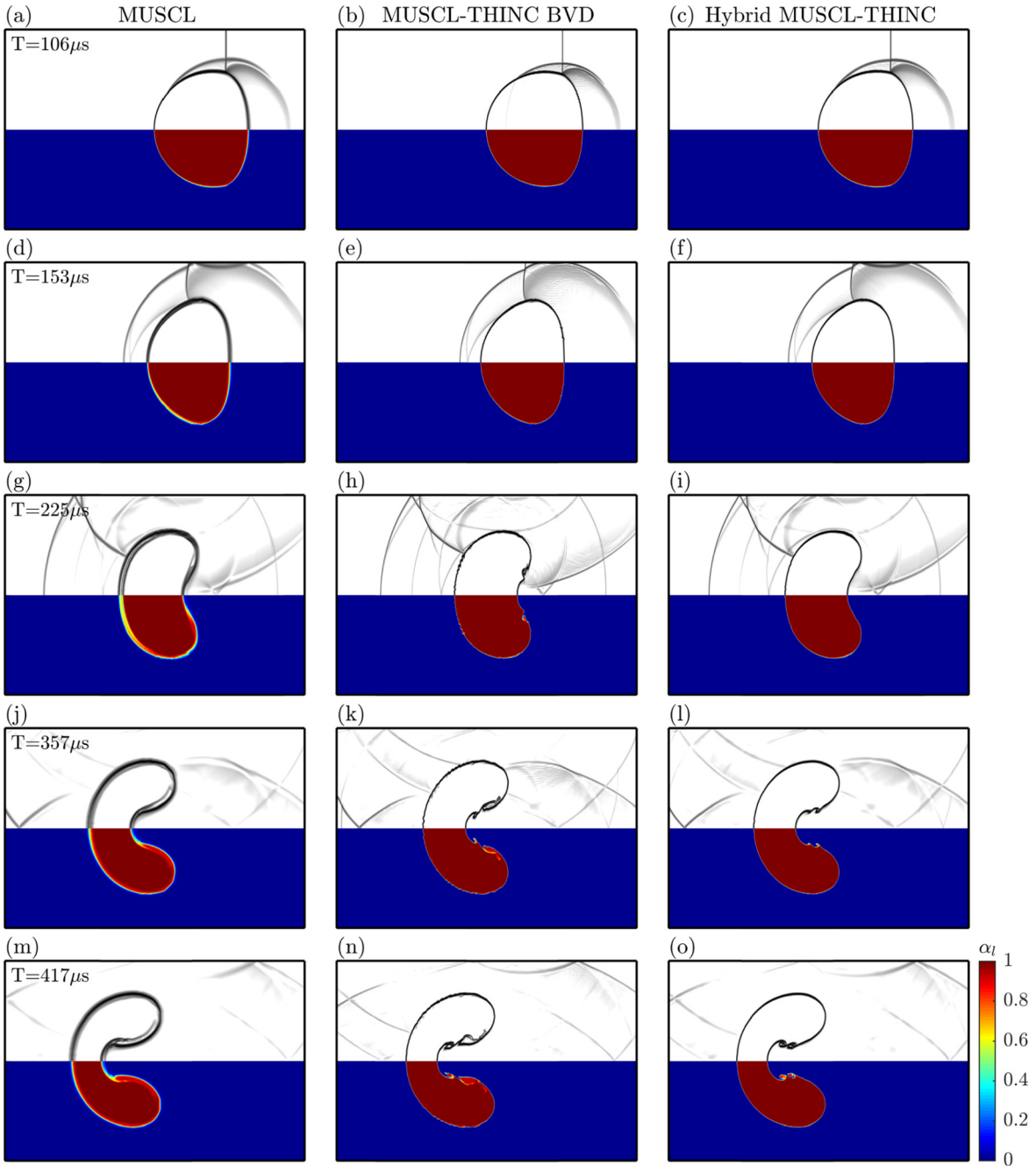


**Fig. 17.** Zoom-in snapshots of the Air/He3 shock bubble interaction obtained by different reconstruction schemes at representative time instants using the initial conditions listed in Table 9. The first column presents results from MUSCL reconstruction, the second column is from MUSCL-THINC BVD, and the third column is from the proposed hybrid MUSCL-THINC scheme. The upper part in each sub-figure is the numerical Schlieren function of the density gradient, while the lower part is the volume fraction of the R22 refrigerant.

and bottom boundaries. The computational time step ( $\Delta t$ ) is fixed such that the CFL number = 0.5. Both the MUSCL and hybrid MUSCL-THINC scheme with  $\beta = 1.6$  are employed. At the beginning of the simulation run, a right-moving shock wave with  $M = 1.51$  is located at  $x = 0.01$  m, and the air bubble is located at the domain center. The problem is challenging for two-fluid modeling because the Riemann solver can give the negative pressure when the strong shock wave impinges the air bubble [12]. Therefore, this becomes an indicator for the evaluation of the current AUSMD-type flux algorithm.

The snapshots of the volume fraction, Schlieren-type image, and the pressure contour for hybrid MUSCL-THINC scheme are presented in Fig. 18. It can be seen that the air bubble begins to deform when the shock wave impinges (see Figs. 18a

**Table 11**

Initial conditions for the problem of water shock air bubble interaction. Here the subscript  $k$  represents either the liquid or gas phase, and  $\epsilon = 10^{-5}$ .

	Behind the shock	Before the shock	Inside the water column	Units
$\alpha_l$	$1 - \epsilon$	$1 - \epsilon$	$\epsilon$	
$p$	$1.6 \times 10^9$	$1.01 \times 10^5$	$1.01 \times 10^5$	Pa
$u_k$	661.81	0	0	$\text{m s}^{-1}$
$v_k$	0	0	0	$\text{m s}^{-1}$
$T_k$	595.13	292.98	292.98	K

**Table 12**

Initial conditions for the problem of the Mach 1.47 shock liquid column interaction. Here, the subscript  $k$  represents either the liquid or gas phase, and  $\epsilon = 10^{-5}$ .

	Behind the shock	Before the shock	Inside the column	Units
$\alpha_g$	$1 - \epsilon$	$1 - \epsilon$	$\epsilon$	
$p$	$2.35 \times 10^5$	$1 \times 10^5$	$1 \times 10^5$	Pa
$u_k$	225.86	0	0	$\text{m s}^{-1}$
$v_k$	0	0	0	$\text{m s}^{-1}$
$T_k$	381.85	293.15	293.15	K

and b). The bubble is then compressed due to the ambient high pressure (see Figs. 18c-f) and subsequently collapses into two segments (see Figs. 18g and h). More details of the phenomenon can be found in Chang and Liou [12]. Our results in Fig. 18 agree well with the previous study using different flux algorithms [12,15,22,28,56], and the negative pressure is not found during the simulations. Moreover, comparison between results using MUSCL and the hybrid MUSCL-THINC scheme can be found in Fig. 19. It can be seen that the material interface and reflection wave obtained by the present hybrid scheme (see first column of Fig. 19) are sharper than those obtained by the MUSCL scheme (see second column of Fig. 19).

### 3.2.6. Mach 1.47 shock liquid column interaction

In this example, we consider a planar shock wave in the gas phase impacting a liquid column of diameter 4.8 mm. This case has been conducted both experimentally [60] and numerically [14,15,22,56,61,62] for examining the early-stage interaction between the shock wave and liquid column. Following Liou et al. [14] and Kitamura and Nonomura [15], the initial conditions are summarized in Table 12.

Computations are conducted in a domain with dimensions  $L_x \times L_y = 0.04 \text{ m} \times 0.04 \text{ m}$  by using a grid resolution of  $N_x \times N_y = 1200 \times 1200$ . A right-moving shock wave with  $M = 1.47$  is set at  $x = 0.01 \text{ m}$ , and the liquid column is located at the domain center. For a comparison with the experimental results obtained by Igra and Takayama [60], we also consider the surface tension acting on the interface (see Eqs. (9) and (10)), and a fixed Weber number ( $We$ ), i.e.,

$$We \equiv \frac{\rho_g u_\infty^2 D}{\sigma} = 6900, \quad (77)$$

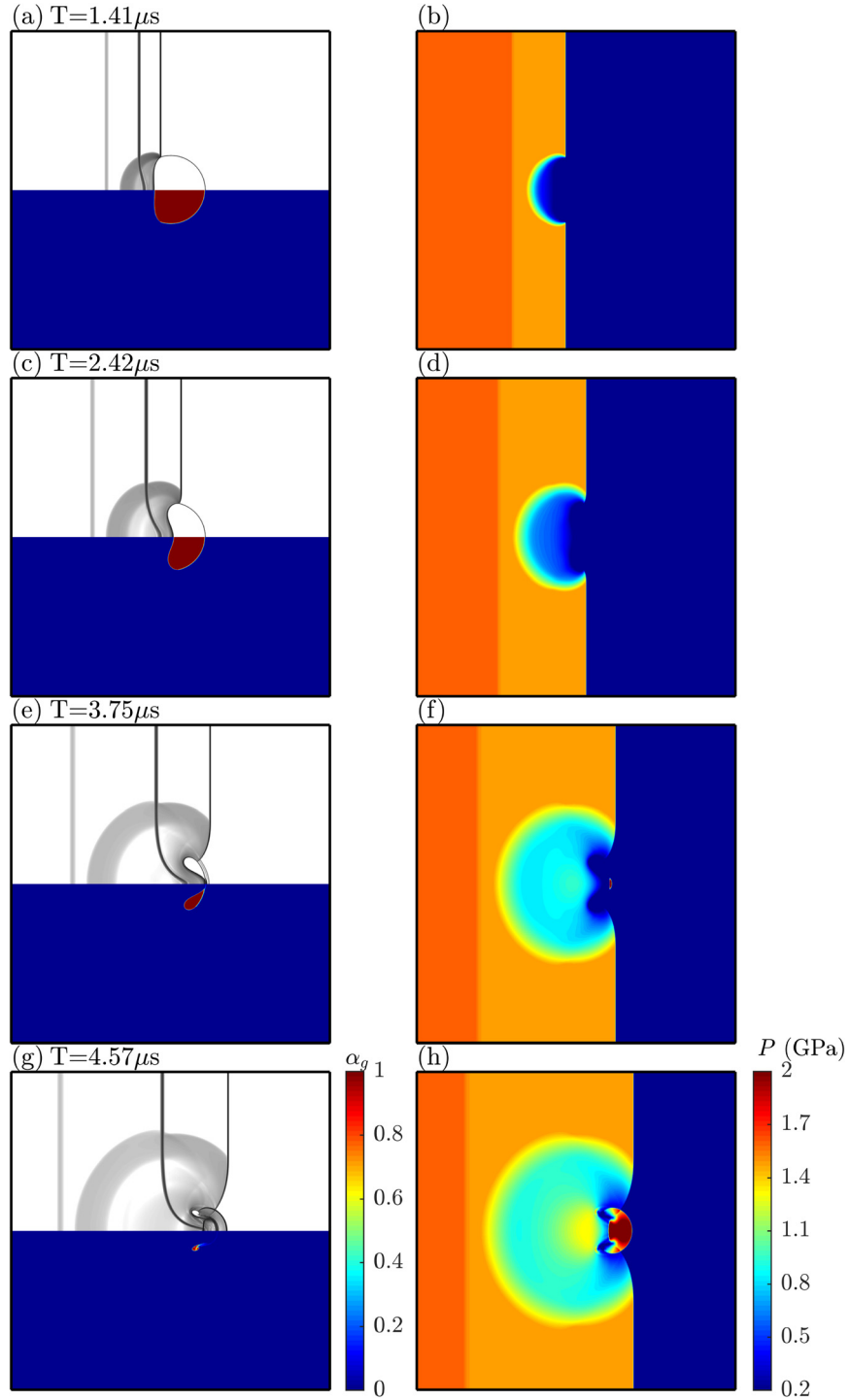
where  $\rho_g$  is the density of gas,  $u_\infty$  is the inlet velocity,  $D$  is the diameter of the liquid column, and  $\sigma$  ( $\text{N m}^{-1}$ ) is the surface tension coefficient. The inlet and outlet conditions are imposed at the left and right boundaries, respectively, and the open boundary condition is imposed at both the top and bottom boundaries. The computational time step ( $\Delta t$ ) is fixed such that the CFL number = 0.4 throughout the simulation.

Fig. 20 shows representative snapshots of the Schlieren function of the density gradient and the volume fraction of the liquid from the results obtained using MUSCL and hybrid MUSCL-THINC with  $\beta = 2.4$ . In the earlier stage (Figs. 20a and b) when the incident shock wave has not yet affected the material interface, the results obtained from the two schemes do not differ significantly. As shown in Figs. 20c-f, after the shock wave passes through the water column, the crossflow induced by the incident shock wave begins to interfere with the interface. Meanwhile, two vortices are generated at the upper and lower sides of the water column. The same flow feature was found by Garrick et al. [61,62].

A comparison among Figs. 20c-h shows that the interface reconstructed by the original MUSCL scheme diffuses from the leading side to the interior region of the liquid column. Although the results obtained from both schemes qualitatively agree with the experimental results obtained in Igra and Takayama [60], the hybrid MUSCL-THINC scheme significantly reduces the interface thickness and captures more details of a small disturbance on the liquid surface. Moreover, Figs. 20g and h show that clearer wave patterns are resolved in the hybrid scheme than those in the MUSCL-only case.

### 3.2.7. Mach 3 shock liquid column interaction

Another example of the planar shock wave impinging on a water column of diameter 10 mm is presented in this section, which is similar to that used in the numerical study conducted by Chang and Liou [12]. Following Chang and Liou [12], the setup of state variables used in this study is summarized in Table 13.



**Fig. 18.** Snapshots of water shock air bubble interaction obtained using the hybrid MUSCL-THINC scheme at representative time instants using the initial conditions listed in Table 11. The first column is the volume fraction of gas (upper panel) and Schlieren function of density gradient (lower panel), and the second column is pressure contour ranging from 0.2 to 2.0 GPa.

Computations are conducted in a domain with dimensions  $L_x \times L_y = 0.09 \text{ m} \times 0.03 \text{ m}$  using grid resolution  $N_x \times N_y = 1800 \times 600$ , and the water column is located at  $(x, y) = (0.03 \text{ m}, 0.02 \text{ m})$ . A right-moving shock wave with  $M = 3$  is initially set to be located at  $x = 0.02 \text{ m}$ . The inlet and outlet conditions are imposed at the left and right boundaries, respectively, and the reflective wall condition is imposed at both the top and bottom boundaries. The computational time step ( $\Delta t$ )

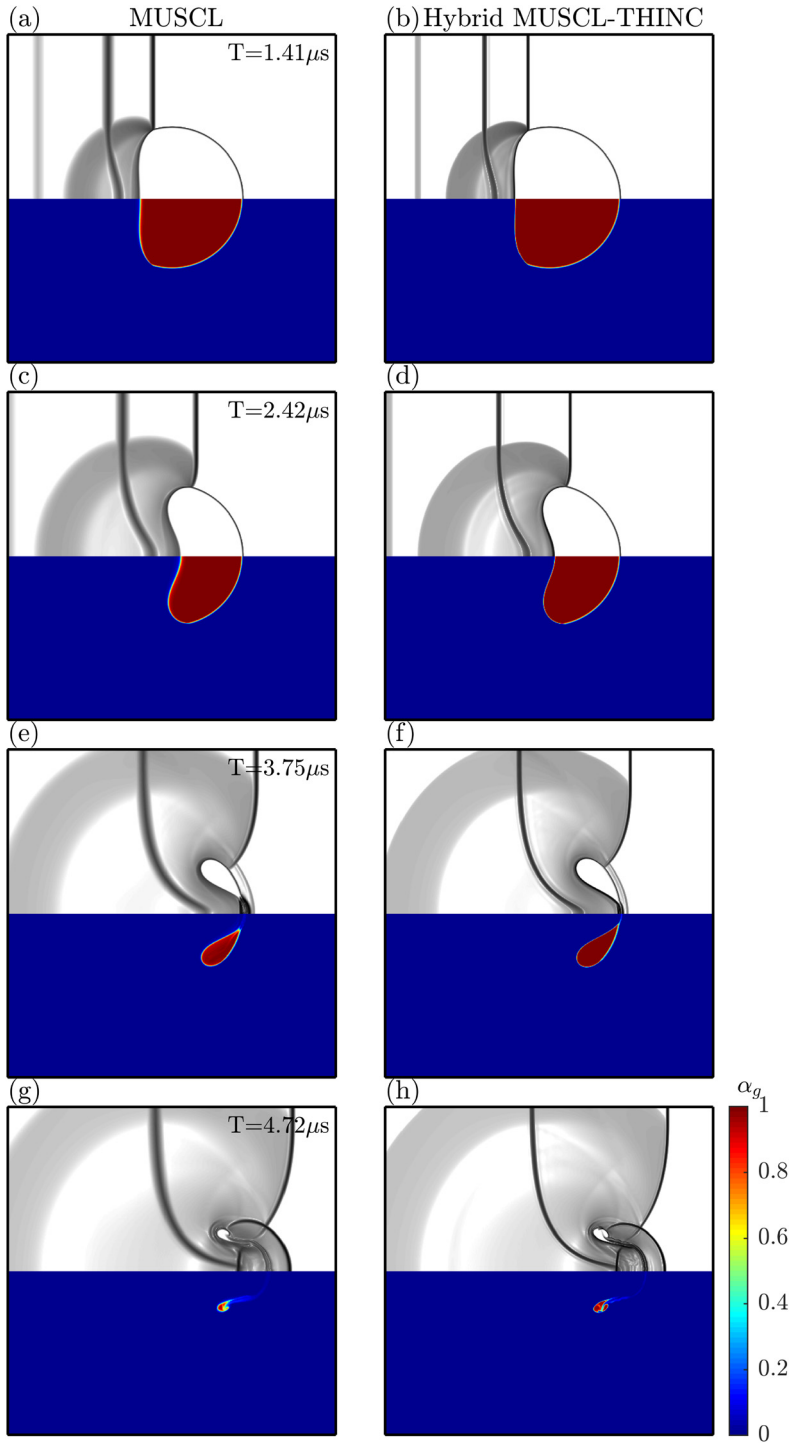


**Fig. 19.** Zoom-in snapshots of water shock air bubble interaction obtained using different reconstruction schemes at representative time instants using the initial conditions listed in Table 11. The first column is results obtained by MUSCL, and the second column is results from the present hybrid MUSCL-THINC scheme. The upper half of each panel is the numerical Schlieren function of density gradient, and the lower half is the volume fraction of gas.

is fixed such that the CFL number = 0.4 throughout the simulation. Again, this case is conducted using both MUSCL and hybrid MUSCL-THINC schemes ( $\beta = 2.0$ ) for a comparison.

Fig. 21 shows representative snapshots of Schlieren-type images for the density gradient and volume fraction of liquid. As shown in the figure, when the incident shock wave impacts the water column, part of the shock wave transmits into the water column, whereas the other part is reflected (see Figs. 21a and b). As shown in Figs. 21c and d, the cavitation zone

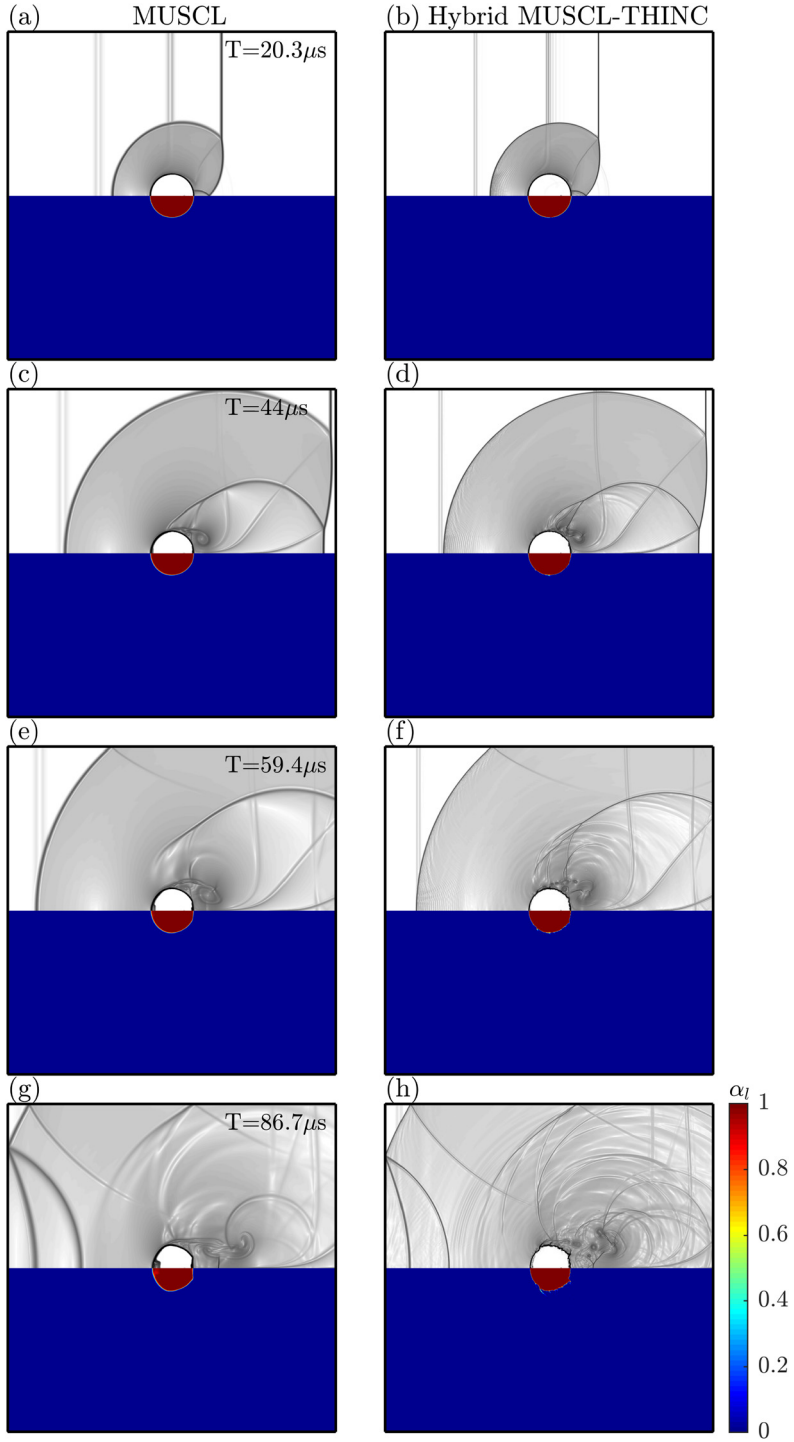


**Fig. 20.** Zoom-in snapshots of Mach 1.47 shock water column interaction with different reconstruction schemes at representative time instants under the initial condition listed in Table 12. The first column is results reconstructed by MUSCL, and the second column is results reconstructed by the proposed hybrid MUSCL-THINC scheme. The upper part of single plot is the numerical Schlieren function of density gradient; The lower part is the volume fraction of liquid.

emerges at the downstream pole of the water column corresponding to the low-pressure region. It shrinks and gradually collapses into a point. Eventually, a secondary shock wave is generated in this region, and then propagates toward the liquid surface (see Figs. 21e and f). Fig. 21 shows that the interface diffuses more in the MUSCL case, particularly during the

**Table 13**

Initial condition for Mach 3 shock liquid column interaction. Here the subscript  $k$  represents either the liquid or gas phase, and  $\epsilon = 10^{-5}$ .

	Behind the shock	Before the shock	Inside the water column	Units
$\alpha_g$	$1 - \epsilon$	$1 - \epsilon$	$\epsilon$	
$p$	$1.03 \times 10^6$	$1 \times 10^5$	$1 \times 10^5$	Pa
$u_k$	831.48	0	0	$\text{m s}^{-1}$
$v_k$	0	0	0	$\text{m s}^{-1}$
$T_k$	929.57	346.98	346.98	K

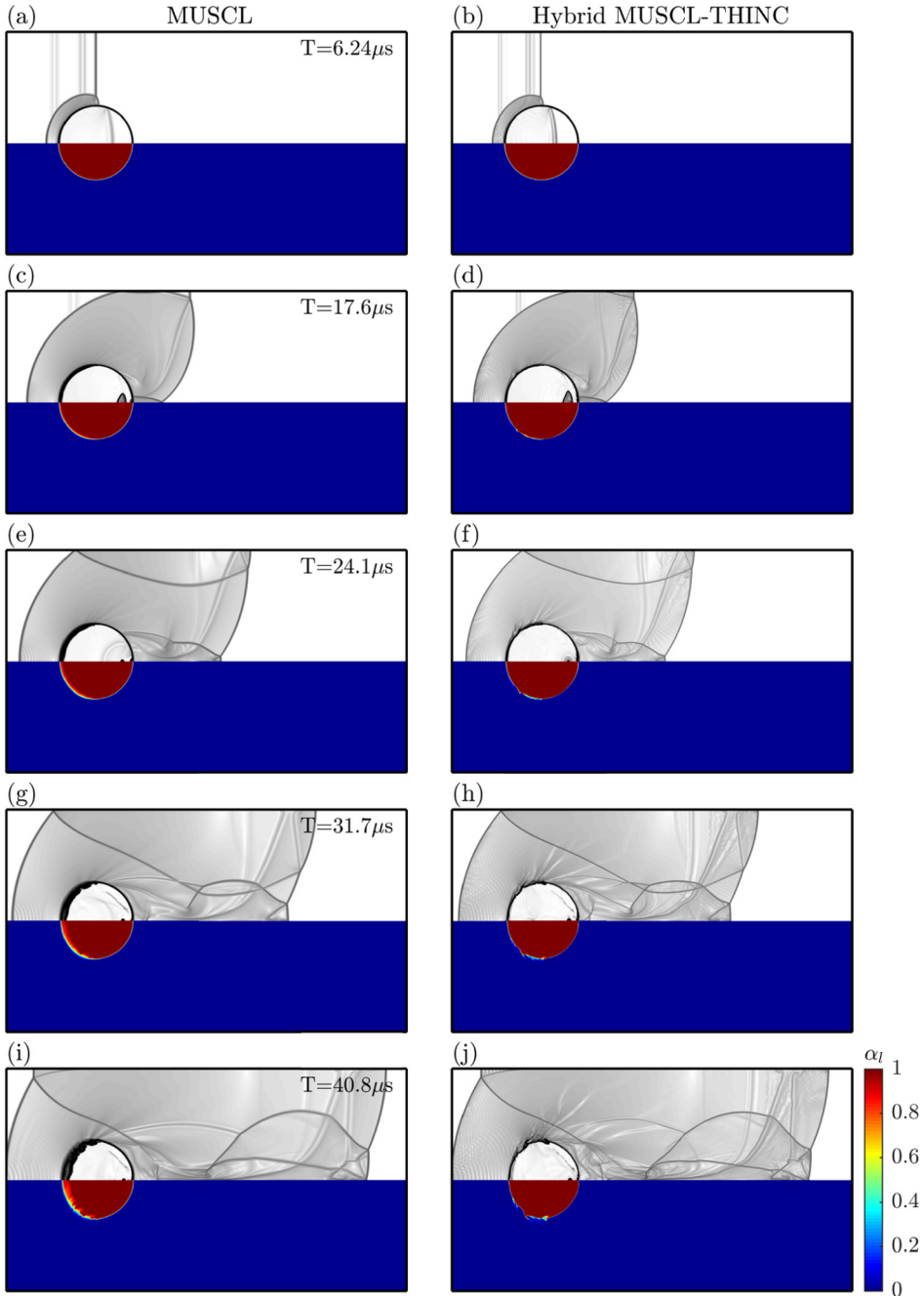


**Fig. 21.** Snapshots of Mach 3 shock water column interaction with different reconstruction scheme at representative time instants under the initial condition listed in Table 13. The first column is results reconstructed by MUSCL, and the second column is results reconstructed by the proposed hybrid MUSCL-THINC scheme. The upper part of single plot is the numerical Schlieren function of density gradient; The lower part is the volume fraction of water.

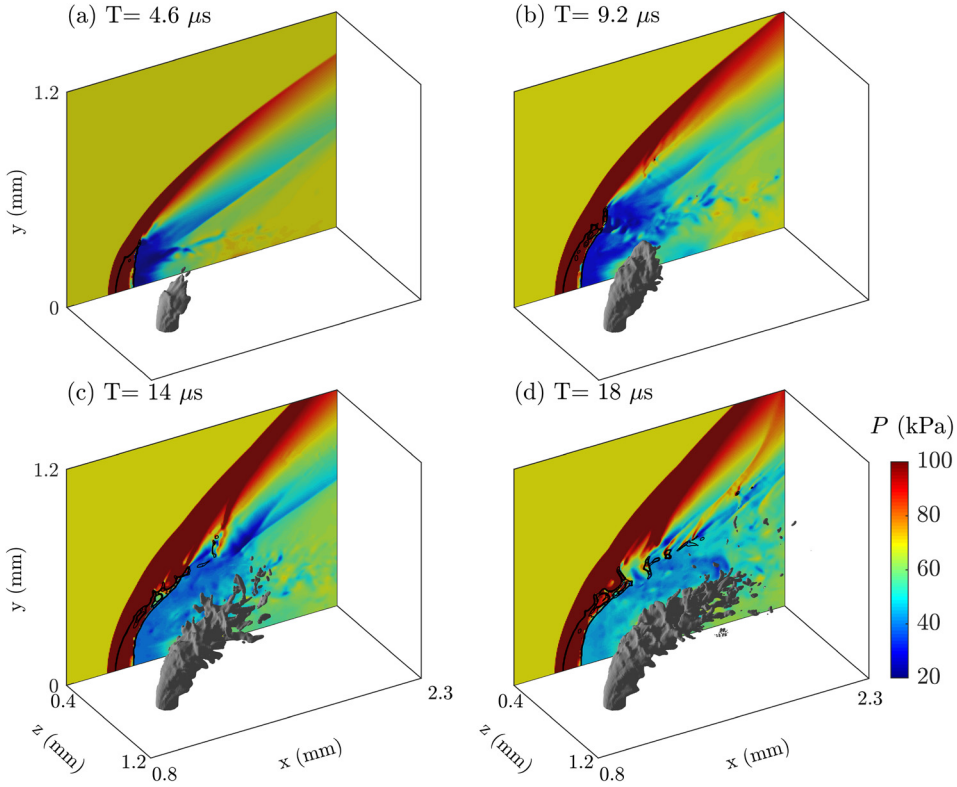


**Fig. 22.** Iso-surfaces of  $\alpha_l = 0.2$  along with the pressure field and contours of  $\alpha_l$  (black lines) at the central slice in the  $z$ -direction of the liquid-jet-crossflow problem using the present hybrid MUSCL-THINC scheme at four representative time instants.

later time stage (e.g., Figs. 21g-j). Moreover, because of the nondiffusive nature of the hybrid MUSCL-THINC scheme, more detailed flow features can be captured by the calculation.

### 3.2.8. Mach 2.1 liquid jet crossflow

As the last numerical example, we implement the present scheme in a 3D case of atomization of a high-speed jet crossflow, which has been extensively studied [61,63,64]. Computations are conducted in a domain with dimensions  $L_x \times L_y \times L_z = 3 \text{ mm} \times 1.5 \text{ mm} \times 1.6 \text{ mm}$  at a grid resolution of  $N_x \times N_y \times N_z = 600 \times 300 \times 320$ . In this case, a liquid jet with a diameter of 0.1 mm is injected into a supersonic crossflow with  $M = 2.1$  [63], and the liquid-to-gas momentum flux ratio  $q$  is set as

$$q = \frac{\rho_l u_l^2}{\rho_g u_g^2} = 4. \quad (78)$$

Following Xiao et al. [63], a fixed  $We$  is set to 594, which corresponds to the surface tension coefficient,  $\sigma = 0.07 \text{ N m}^{-1}$ . The inlet and outlet conditions are applied at the left and right ends of the domain, respectively. The no-penetration condition is used at the bottom boundary, except at the jet orifice, where the inlet condition is imposed, whereas the open boundary condition is enforced on the remaining boundaries. The computational time step ( $\Delta t$ ) is fixed such that the CFL number = 0.4 throughout the simulation. Because the viscous effect is neglected in this study, we skip the near-wall region and only focus on the interfacial behavior between the liquid jet and ambient gas, where viscosity is less important.

Fig. 22 presents the simulation results obtained using the hybrid MUSCL-THINC scheme with  $\beta = 2.4$ . Figs. 22a and b show that upon leaving the jet orifice, the bow shock is formed ahead of the liquid column. This generates a near-field pressure gradient and bends the liquid jet in the streamwise direction. As shown in Fig. 22c, the surface wave can be observed on the windward side of the liquid jet, followed by breakup of the liquid jet into clusters of droplets. Although the viscous effect is not included here, it can be found that the flow structures on the interfacial region of the liquid jet (e.g., surface wave and droplet) agree well with simulation results in Xiao et al. [63] and the experimental observation in Wang et al. [65], where the same air flow conditions are specified.

Comparison between Figs. 23a and c shows that when  $We$  becomes lower (i.e., higher surface tension), the liquid–gas interface can be more stabilized, and small segments resulting from the breakup of the interface are found further downstream from the orifice. Unlike the present hybrid MUSCL-THINC scheme which shows detailed interfacial flow structures

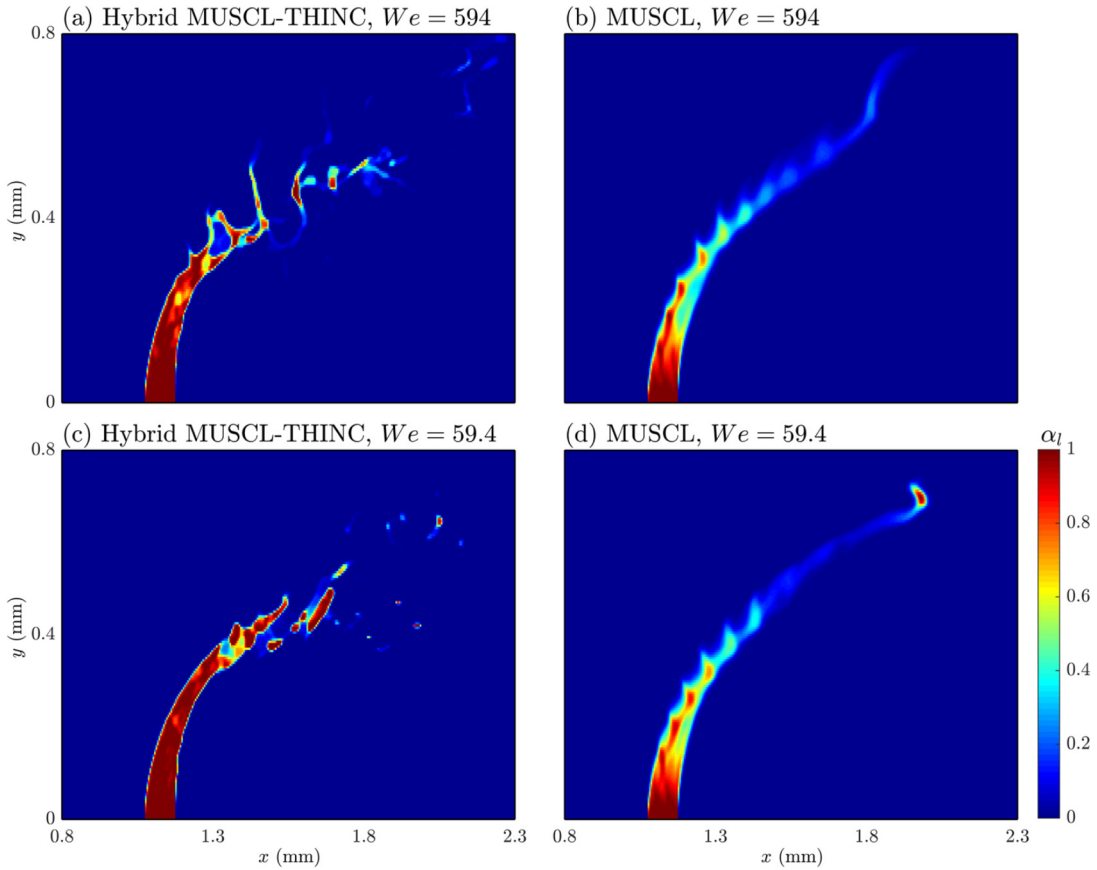


**Fig. 23.** Volume fraction of liquid ( $\alpha_l$ ) at the central slice in the  $z$ -direction of the Mach 2.1 liquid-jet-crossflow problem with  $We = 594$  and  $We = 59.4$  at  $T = 19\mu s$ . The first column is results reconstructed by hybrid MUSCL-THINC scheme, and the second column is results reconstructed by MUSCL scheme.

(see Figs. 23a and c), formation of small droplets cannot be found in the MUSCL-only case (see Figs. 23b and d). This can be attributed to the increased thickness of the interface in the MUSCL-only case, which stabilizes the interface, thus preventing the interfacial waves from breaking. Here, it is demonstrated that retaining the sharpness of the interface is crucial while accounting for the surface tension, and the proposed hybrid scheme is able to give satisfactory results.

#### 4. Conclusions

In this study, a hybrid AUSMD flux reconstruction algorithm is developed for the simulation of multiphase flows, in which the interface between different fluid phases inside a grid cell is reconstructed using the stratified flow model [12,23]. In this flux reconstruction scheme, the mass flux and pressure are calculated using an approximate Riemann solver (e.g., PVRS), such that lesser computational cost is required than that required for an exact Riemann solver. Moreover, a hybrid MUSCL-THINC scheme is presented for interpolating the values of state variables at the cell faces. In this scheme, a slope-weighted parameter is devised to determine the relative weight of THINC (for sharp variations) and MUSCL (for smooth variations) depending on the discontinuity of the variable field. Unlike most existing schemes, which apply only THINC to the volume fraction of different phases, the present scheme, when applied to all physical variables, provides robust and accurate computations for multiphase flow simulations. Furthermore, a series of benchmark numerical tests are conducted, and the results show that the proposed scheme can maintain the sharpness and discontinuity resulting from the shock waves and fluid interfaces. Because the proposed scheme can substantially suppress the numerical diffusion, important flow features at the fluid interfaces, such as interfacial instabilities and breakup phenomena, can be reproduced in greater detail in the examples of 2D shock–bubble interactions and 3D liquid jet crossflow.

#### CRediT authorship contribution statement

**Te-Yao Chiu:** Conceptualization, Investigation, Methodology, Programming, Visualization, Writing – original draft. **Yang-Yao Niu:** Conceptualization, Investigation, Methodology, Supervision, Writing – review. **Yi-Ju Chou:** Conceptualization, Investigation, Methodology, Resources, Funding acquisition, Writing – review and editing.

## Declaration of competing interest

The authors declare that they have no known competing financial interests or personal relationships that could have appeared to influence the work reported in this paper.

## Acknowledgements

We gratefully acknowledge the support of the Taiwan Ministry of Science and Technology (MOST) Thermal Science and Fluid Dynamic Program under Grant No. MOST 109-2221-E-002-028-MY3, the Ministry of Education (MOE) Higher Education Sprout Project in Taiwan (NTU Core Consortium: 108L880206), and National Taiwan University career development project (NTU-CDP-108L7720). The computation was performed on the Dell PowerEdge M620 supercomputer cluster located at Center of Advanced Study Theoretical Sciences at National Taiwan University, which is gratefully acknowledged.

## References

- [1] A. Murrone, H. Guillard, A five equation reduced model for compressible two phase flow problems, *J. Comput. Phys.* 202 (2005) 664–698.
- [2] G. Allaire, S. Clerc, S. Kokh, A five-equation model for the simulation of interfaces between compressible fluids, *J. Comput. Phys.* 181 (2002) 577–616.
- [3] C. Hirt, B. Nichols, Volume of fluid (VoF) method for the dynamics of free boundaries, *J. Comput. Phys.* 39 (1981) 201–225.
- [4] A.Q. Raeini, M.J. Blunt, B. Bijeljic, Modelling two-phase flow in porous media at the pore scale using the volume-of-fluid method, *J. Comput. Phys.* 231 (2012) 5653–5668.
- [5] S. Osher, J.A. Sethian, Fronts propagating with curvature-dependent speed: algorithms based on Hamilton-Jacobi formulations, *J. Comput. Phys.* 79 (1988) 12–49.
- [6] M. Sussman, P. Smereka, S. Osher, A level set approach for computing solutions to incompressible two-phase flow, *J. Comput. Phys.* 114 (1994) 146–159.
- [7] H. Kim, M.-S. Liou, Accurate adaptive level set method and sharpening technique for three dimensional deforming interfaces, *Comput. Fluids* 44 (2011) 111–129.
- [8] M. Baer, J. Nunziato, A two-phase mixture theory for the deflagration-to-detonation transition (DDT) in reactive granular materials, *Int. J. Multiph. Flow* 12 (1986) 861–889.
- [9] R. Saurel, R. Abgrall, A multiphase Godunov method for compressible multifluid and multiphase flows, *J. Comput. Phys.* 150 (1999) 425–467.
- [10] M. Ishii, *Thermo-Fluid Dynamic Theory of Two-Phase Flow*, Eyrolles, Paris, France, 1975.
- [11] D.A. Drew, Mathematical modeling of two-phase flow, *Annu. Rev. Fluid Mech.* 15 (1983) 261–291.
- [12] C.-H. Chang, M.-S. Liou, A robust and accurate approach to computing compressible multiphase flow: stratified flow model and AUSM+-up scheme, *J. Comput. Phys.* 225 (2007) 840–873.
- [13] Y.-Y. Niu, Computations of two-fluid models based on a simple and robust hybrid primitive variable Riemann solver with AUSMD, *J. Comput. Phys.* 308 (2016) 389–410.
- [14] M.-S. Liou, C.-H. Chang, L. Nguyen, T.G. Theofanous, How to solve compressible multifluid equations: a simple, robust, and accurate method, *AIAA J.* 46 (2008) 2345–2356.
- [15] K. Kitamura, T. Nonomura, Simple and robust HLLC extensions of two-fluid AUSM for multiphase flow computations, *Comput. Fluids* 100 (2014) 321–335.
- [16] F. Xiao, Y. Honma, T. Kono, A simple algebraic interface capturing scheme using hyperbolic tangent function, *Int. J. Numer. Methods Fluids* 48 (2005) 1023–1040.
- [17] J. Stuhmller, The influence of interfacial pressure forces on the character of two-phase flow model equations, *Int. J. Multiph. Flow* 3 (1977) 551–560.
- [18] D. Drew, L. Cheng, R. Lahey Jr, The analysis of virtual mass effects in two-phase flow, *Int. J. Multiph. Flow* 5 (1979) 233–242.
- [19] D. Lhuillier, C.-H. Chang, T.G. Theofanous, On the quest for a hyperbolic effective-field model of disperse flows, *J. Fluid Mech.* 731 (2013) 184–194.
- [20] I. Toumi, A. Kumbaro, An approximate linearized Riemann solver for a two-fluid model, *J. Comput. Phys.* 124 (1996) 286–300.
- [21] H. Paillere, C. Corre, J.G. Cascales, On the extension of the AUSM+-up scheme to compressible two-fluid models, *Comput. Fluids* 32 (2003) 891–916.
- [22] K. Kitamura, M.-S. Liou, C.-H. Chang, Extension and comparative study of AUSM-family schemes for compressible multiphase flow simulations, *Comput. Phys.* 16 (2014) 632–674.
- [23] H.B. Stewart, B. Wendroff, Two-phase flow: models and methods, *J. Comput. Phys.* 56 (1984) 363–409.
- [24] M.-S. Liou, A sequel to AUSM, part II: AUSM+-up for all speeds, *J. Comput. Phys.* 214 (2006) 137–170.
- [25] M.-S. Liou, A sequel to AUSM: AUSM+, *J. Comput. Phys.* 129 (1996) 364–382.
- [26] E.F. Toro, *Riemann Solvers and Numerical Methods for Fluid Dynamics: A Practical Introduction*, Springer, Berlin Heidelberg, Berlin, Heidelberg, 2009.
- [27] A.K. Pandare, H. Luo, A robust and efficient finite volume method for compressible inviscid and viscous two-phase flows, *J. Comput. Phys.* 371 (2018) 67–91.
- [28] A.K. Pandare, H. Luo, J. Bakosi, An enhanced AUSM+-up scheme for high-speed compressible two-phase flows on hybrid grids, *Shock Waves* 29 (2019) 629–649.
- [29] R.W. Houim, E.S. Oran, A multiphase model for compressible granular-gaseous flows: formulation and initial tests, *J. Fluid Mech.* 789 (2016) 166.
- [30] Y. Wada, M.-S. Liou, An accurate and robust flux splitting scheme for shock and contact discontinuities, *SIAM J. Sci. Comput.* 18 (1997) 633–657.
- [31] E. Toro, A linearized Riemann solver for the time-dependent Euler equations of gas dynamics, *Proc. R. Soc. Lond. Ser. A, Math. Phys. Sci.* 434 (1991) 683–693.
- [32] Y.-Y. Niu, H.-W. Wang, Simulations of the shock waves and cavitation bubbles during a three-dimensional high-speed droplet impingement based on a two-fluid model, *Comput. Fluids* 134 (2016) 196–214.
- [33] B. Van Leer, Towards the ultimate conservative difference scheme. V. A second-order sequel to Godunov's method, *J. Comput. Phys.* 32 (1979) 101–136.
- [34] R.K. Shukla, C. Pantano, J.B. Freund, An interface capturing method for the simulation of multi-phase compressible flows, *J. Comput. Phys.* 229 (2010) 7411–7439.
- [35] R.K. Shukla, Nonlinear preconditioning for efficient and accurate interface capturing in simulation of multicomponent compressible flows, *J. Comput. Phys.* 276 (2014) 508–540.
- [36] K. So, X. Hu, N.A. Adams, Anti-diffusion interface sharpening technique for two-phase compressible flow simulations, *J. Comput. Phys.* 231 (2012) 4304–4323.
- [37] S. Tann, X. Deng, Y. Shimizu, R. Loubère, F. Xiao, Solution property preserving reconstruction for finite volume scheme: a bvd+ mood framework, *Int. J. Numer. Methods Fluids* (2019).
- [38] Z. Sun, S. Inaba, F. Xiao, Boundary variation diminishing (BVD) reconstruction: a new approach to improve Godunov schemes, *J. Comput. Phys.* 322 (2016) 309–325.

- [39] X. Deng, B. Xie, R. Loubère, Y. Shimizu, F. Xiao, Limiter-free discontinuity-capturing scheme for compressible gas dynamics with reactive fronts, *Comput. Fluids* 171 (2018) 1–14.
- [40] X. Deng, Y. Shimizu, F. Xiao, A fifth-order shock capturing scheme with two-stage boundary variation diminishing algorithm, *J. Comput. Phys.* 386 (2019) 323–349.
- [41] X. Deng, S. Inaba, B. Xie, K.-M. Shyue, F. Xiao, High fidelity discontinuity-resolving reconstruction for compressible multiphase flows with moving interfaces, *J. Comput. Phys.* 371 (2018) 945–966.
- [42] Y.-Y. Niu, Y.-C. Chen, T.-Y. Yang, F. Xiao, Development of a less-dissipative hybrid AUSMD scheme for multi-component flow simulations, *Shock Waves* 29 (2019) 691–704.
- [43] L. Cheng, X. Deng, B. Xie, Y. Jiang, F. Xiao, Low-dissipation BVD schemes for single and multi-phase compressible flows on unstructured grids, *J. Comput. Phys.* 428 (2021) 110088.
- [44] L.D. Landau, E.M. Lifshitz, *Fluid Mechanics*, vol. 6, second ed., Pergamon, 1987.
- [45] J.U. Brackbill, D.B. Kothe, C. Zemach, A continuum method for modeling surface tension, *J. Comput. Phys.* 100 (1992) 335–354.
- [46] F. Harlow, A. Amsden, Fluid dynamics, technical report la-4700, Los Alamos National Laboratory, 1971.
- [47] S. Jolgam, A. Ballil, A. Nowakowski, F. Nicolleau, On equations of state for simulations of multiphase flows, in: *World Congress on Engineering 2012, July 4–6, 2012, London, UK*, vol. 3, International Association of Engineers, London, UK, 2012, pp. 1963–1968.
- [48] G.-S. Jiang, C.-W. Shu, Efficient implementation of weighted ENO schemes, *J. Comput. Phys.* 126 (1996) 202–228.
- [49] G.A. Sod, A survey of several finite difference methods for systems of nonlinear hyperbolic conservation laws, *J. Comput. Phys.* 27 (1978) 1–31.
- [50] P. Woodward, P. Colella, The numerical simulation of two-dimensional fluid flow with strong shocks, *J. Comput. Phys.* 54 (1984) 115–173.
- [51] X. Deng, Y. Shimizu, B. Xie, F. Xiao, Constructing higher order discontinuity-capturing schemes with upwind-biased interpolations and boundary variation diminishing algorithm, *Comput. Fluids* 200 (2020) 104433.
- [52] M. Pandolfi, D. D'Ambrosio, Numerical instabilities in upwind methods: analysis and cures for the “carbuncle” phenomenon, *J. Comput. Phys.* 166 (2001) 271–301.
- [53] N. Fleischmann, S. Adami, N.A. Adams, A shock-stable modification of the HLLC Riemann solver with reduced numerical dissipation, *J. Comput. Phys.* 423 (2020) 109762.
- [54] S. Simon, J. Mandal, A simple cure for numerical shock instability in the HLLC Riemann solver, *J. Comput. Phys.* 378 (2019) 477–496.
- [55] S.-s. Chen, C. Yan, B.-x. Lin, L.-y. Liu, J. Yu, Affordable shock-stable item for Godunov-type schemes against carbuncle phenomenon, *J. Comput. Phys.* 373 (2018) 662–672.
- [56] T. Nonomura, K. Kitamura, K. Fujii, A simple interface sharpening technique with a hyperbolic tangent function applied to compressible two-fluid modeling, *J. Comput. Phys.* 258 (2014) 95–117.
- [57] P. Dimotakis, R. Samtaney, Planar shock cylindrical focusing by a perfect-gas lens, *Phys. Fluids* 18 (2006) 031705.
- [58] R.D. Richtmyer, Taylor instability in shock acceleration of compressible fluids, *Commun. Pure Appl. Math.* 13 (1960) 297–319.
- [59] E. Meshkov, Instability of a shock wave accelerated interface between two gases, *NASA Tech. Trans.* 13 (1970) 74.
- [60] D. Igra, K. Takayama, Investigation of aerodynamic breakup of a cylindrical water droplet, *At. Sprays* 11 (2001).
- [61] D.P. Garrick, W.A. Hagen, J.D. Regele, An interface capturing scheme for modeling atomization in compressible flows, *J. Comput. Phys.* 344 (2017) 260–280.
- [62] D.P. Garrick, M. Owkes, J.D. Regele, A finite-volume HLLC-based scheme for compressible interfacial flows with surface tension, *J. Comput. Phys.* 339 (2017) 46–67.
- [63] F. Xiao, Z. Wang, M. Sun, J. Liang, N. Liu, Large eddy simulation of liquid jet primary breakup in supersonic air crossflow, *Int. J. Multiph. Flow* 87 (2016) 229–240.
- [64] K. Mahesh, The interaction of jets with crossflow, *Annu. Rev. Fluid Mech.* 45 (2013) 379–407.
- [65] Z.-g. Wang, L. Wu, Q. Li, C. Li, Experimental investigation on structures and velocity of liquid jets in a supersonic crossflow, *Appl. Phys. Lett.* 105 (2014) 134102.